Journal of Geophysical Research: Oceans
DOI 10.1002/jgrc.20232

Physical and biogeochemical properties in landfast sea ice (Barrow, Alaska): insights on brine and gas dynamics across seasons

Authors Jiayun Zhou[1,2*], Bruno Delille[2], Hajo Eicken[3], Martin Vancoppenolle[4], Frédéric Brabant[1], Gauthier Carnat[5], Nicolas-Xavier Geilfus[5], Tim Papakyriakou[5], Bernard Heinesch[6] and Jean-Louis Tison[1]

[1] Laboratoire de glaciologie, DSTE, Université Libre de Bruxelles, Belgium

[2] Unité d'océanographie chimique, MARE, Université de Liège, Belgium

[3] Geophysical Institute, University of Alaska Fairbanks, United States

[4] Laboratoire d'Océanographie et du Climat, CNRS, France

[5] Department of Environment and Geography, CEOS, University of Manitoba, Canada

[6] Unité de physique des biosystèmes, Gembloux Agro-Bio Tech, Université de Liège, Belgium

* Corresponding author e-mail: jiayzhou@ulb.ac.be

Abstract

The impacts of the seasonal evolution of sea-ice physical properties on ice-ocean biogeochemical exchanges were investigated in landfast ice at Barrow (Alaska) from January through June 2009. Three stages of brine dynamics across the annual cycle have been identified based on brine salinity, brine volume fraction and porous medium Rayleigh number

Received: Aug 19, 2012; Revised: Apr 22, 2013; Accepted: May 05, 2013

(Ra). These are sea-ice bottom-layer convection, full-depth convection and brine stratification. We further discuss the impact of brine dynamics on biogeochemical compounds in sea ice: stable isotopes of water (δD, $\delta^{18}O$), nutrients (NO_3^-, PO_4^{3-}, NH_4^+), micro-algae (chlorophyll-a) and inert gas (argon). In general, full-depth convection events favour exchanges between sea ice and seawater, while brine stratification limits these exchanges. However, argon responds differently to brine dynamics than the other biogeochemical compounds analysed in this study. This contrast is attributed to the impact of bubble nucleation on inert gas transport compared to the other biogeochemical compounds. We present a scenario for argon bubble formation and evolution in sea ice and suggest that a brine volume fraction approaching 7.5 % to 10 % is required for inert gas bubbles to escape from sea ice to the atmosphere.

Keywords: Barrow, sea ice, brine, Ra, isotope, nutrient, chlorophyll-a, argon

1. Introduction

Sea ice covers up to 6 % of the Earth's Oceans at its maximum extent [*Comiso*, 2010]. Beside its effects on albedo, polar water mass stratification and vertical mixing, and heat and moisture exchange between the atmosphere and the ocean [*Dieckmann and Hellmer*, 2010], sea ice also plays a key role in the polar marine ecosystem [e.g., *Eicken*, 1992; *Lizotte*, 2001]. It has been shown that the ice cover hosts microbial communities during the winter and spring [e.g., *Horner et al.*, 1992; *Thomas and Dieckmann*, 2002]. It is also well established that sea ice melting in summer frequently triggers phytoplankton blooms at retreating sea ice margins [*Smith and Nelson*, 1986]. In contrast, exchanges between sea ice and seawater and their impact on biota before the melt season are less well documented.

As sea ice forms, impurities (e.g. salt and micro-organisms) in seawater are trapped in brine liquid inclusions within the ice [*Petrich and Eicken*, 2010]. Both ice temperature and salinity control the brine volume fraction [*Cox and Weeks*, 1983; *Hunke et al.*, 2011] and therefore the connectivity of the brine network. Columnar ice permeability in the vertical direction increases drastically for fluid transport when the brine volume fraction exceeds approximately 5 % [*Golden et al.*, 1998; *Pringle et al.*, 2009].

Recent modelling studies suggest a direct link between brine convection (also referred as gravity drainage or convective overturning [*Notz and Worster*, 2009; *Notz et al.*, 2005]) and sea ice biogeochemistry. For instance, *Vancoppenolle et al.* [2010] have shown how brine convection ensures nutrient supply from seawater to sea ice, therefore controlling sea ice algal growth. Experimental studies suggest that unstable brine density profiles lead to convection in permeable sea ice. The porous-medium Rayleigh number (Ra) is an indicator of the propensity of brine convection to occur [*Notz and Worster*, 2008]. Convection is found once Ra exceeds a critical value, typically 10 for young sea ice [*Notz and Worster*, 2008]. When convection develops near the ice bottom, exchanges between sea ice and the underlying seawater occur [e.g., *Niedrauer and Martin*, 1979; *Notz and Worster*, 2008; 2009; *Weeks*, 2010]. Field studies also suggest that convective processes are necessary to explain changes observed in biogeochemical measurements [*Fritsen et al.*, 1994; *Lannuzel et al.*, 2008; *Tison et al.*, 2008], although no obvious link has yet been established between convection process and changes in sea ice biogeochemistry.

In this paper, we provide an integrated view of the link between sea ice physical properties and sea ice biogeochemistry. First, we combine field measurements and parameters derived from experimental studies for assessing ice permeability and brine convection; we examine changes in brine salinity and brine volume fraction in relation to changes in Ra. Second, we

discuss the impact of permeability and convection processes on different biogeochemical compounds in sea ice (and specifically within the brine). The biogeochemical compounds were selected in order to cover impurities existing in different phases in sea ice: liquid (stable isotopes of water, nutrients), solid (chlorophyll-a) and gaseous (argon).

2. Material and methods

2.1 Study site and sampling scheme

The study took place at Barrow, in Alaska, in collaboration with the International Polar Year Seasonal Ice Zone Observing Network (SIZONet) project (www.sizonet.org). The sampling was performed within a 2500 m² square. The north-eastern corner of the square was located at 71° 22.013' N, 156° 32.447' W, 40 m away from the ice mass balance buoy of the Barrow sea ice observatory of the Geophysical Institute (University of Alaska Fairbanks) [*Druckenmiller et al.*, 2009] (Figure 1). The sampling period covered the ice-growth period and melt onset, from January through June 2009. Figure 2 relates the dates of the 10 sampling events (BRW1 to BRW10) to the evolution of air temperature, snow depth and sea ice thickness monitored at the Barrow Sea Ice observatory (data available at seaice.alaska.edu/gi/data). The ice cores were obtained in level landfast first-year sea ice using an electropolished stainless steel corer. Each sampling event took place within an area of 10 m by 10 m. Landfast ice at this site is immobile and is more homogeneous than drifting pack ice. It is thus better suited for temporal studies, because most of the contrasts between samples can be attributed to the temporal evolution rather than the spatial variability [*Druckenmiller et al.*, 2009]. Directly after extraction, the ice cores were stored and kept at -35 °C in the dark. This ensures brine and gas immobilization and inhibits biological activity. Sea ice freeboard was positive during the whole sampling period. Water depth was 9 m. We collected seawater at the ice/seawater interface, 1 m and 6 m below the ice cover.

2.2 Thin sections

Thin sections show ice crystal texture and bubble content. They provide information about the conditions during sea ice formation [*Weeks*, 2010]. The preparation and analysis of thin sections took place in a cold room that was held at -25 °C. 1.5 cm-thick vertical ice core sections were cut using a band saw, then subdivided into 5 cm to 8 cm-long sections. Each section was then stuck on a glass plate, by freezing a small amount of distilled water (4 °C) along its perimeter. Ice sections were thinned to a few millimetres, using a microtome (Leica SM2400). They were then detached from the glass plate by controlled warming, turned over and re-attached through melting and refreezing of a thin interfacial film that does not alter the ice crystallographic properties. Ice sections were then thinned down to 700 µm. The sections were examined between crossed polarisers and photographs were obtained on the Universal Stage system [*Langway*, 1958].

2.3 Ice temperature and salinity

Ice temperature was measured using a calibrated probe (Testo 720). The probe was inserted into holes (matching the diameter of the probe) drilled perpendicular to the ice core axis with a depth resolution of 5 cm. Precision of the probe was +/-0.1 °C. Though temperature measurements were completed within 5 minutes after ice core extraction as recommended by *Pringle and Ingham* [2009], some temperature measurements on extracted ice cores were still depressed towards the air temperature near cracked or open-faced ends of the core (Figure 3). This contrasts with the smooth profiles measured by the in situ thermistors (40 m away from our sampling area). The mean temperature difference between in-situ thermistors and our own temperature profiles was 0.1 °C with a standard deviation of 0.6 °C. The temperature measurements were therefore smoothed to reduce small-scale temperature deviations which we assume to be artefacts of the core extraction and measurement process. Remaining

differences between the smoothed temperatures and those measured by in situ thermistors could be due to differences in snow thickness. Since ice temperatures impact both sea ice physical and biogeochemical properties, we felt more appropriate to use the smoothed temperatures (Figure 5a) in the calculations of brine salinity, brine volume fraction, Ra and argon solubility (See next sections). Contour plots of physical parameters were created using Surfer® package ("natural neighbour" method).

Bulk ice salinity measurements were performed on 5 cm vertical core sections obtained from the ice core that was used for temperature measurements. The core was immediately sectioned in the field, stored in polyethylene containers and left to melt in the Barrow facility laboratories. Salinities were measured with a portable conductimeter (Orion Star Series Meter WP-84TP) on melted ice samples, at room temperature. The precision was +/-0.1.

2.4 Brine volume fraction and brine salinity

Sackholes were drilled into the ice floe surface down to 30 cm, 75 cm and 95 cm depth, to allow gravity-driven brine collection [*Thomas et al.*, 2010]. Each sackhole remained covered with a plastic lid to minimize atmospheric contamination. Brines were collected after 15 minutes to 45 minutes (depending on percolation rate) using a portable peristaltic pump (Master Flex®, E/S portable sampler) and were used for brine salinity, stable isotopes of water, chlorophyll-a and nutrient analyses. Theoretical brine volume fraction and brine salinity were calculated from ice temperature and bulk salinity, neglecting the air volume fraction and using the relationships of *Cox and Weeks* [1983].

2.5 Rayleigh number

Rayleigh number (Ra) is used as a proxy for gravity drainage (i.e. brine convection). Ra expresses the ratio between the negative buoyancy in the brines and dissipation [*Notz and Worster*, 2008]. At a given depth z within sea ice, Ra is given by:

$$Ra = \frac{g \cdot (h_i - z) \cdot \rho_w . \beta_w . [\sigma(z) - S_w] \cdot \Pi(e_{min})}{\kappa \cdot \eta} \quad (1)$$

where g is the gravity acceleration g = 9.81 m·s^{-2}, [$\sigma(z)$-S_w] is the difference between the brine density at the level z and that at the ice-seawater interface, ρ_w is the density of pure water, β_w is the haline expansion coefficient of seawater, with both ρ_w and β_w taken at 0 °C from *Fofonoff* [1985]. $\Pi(e_{min})$ is the effective ice permeability (m²) which is computed using the formula of *Freitag* [1999] (eq. 2.19, p. 48) as a function of the minimum brine volume e_{min} between the level z and the ice-ocean interface. For brine volume fraction, we used the equations given in *Notz and Worster* [2009]. The dynamic viscosity and the thermal diffusivity of brine are η = 2.55 · 10^{-3} kg·(m·s)$^{-1}$ and κ = 1.2 · 10^{-7} m·s^{-2}, respectively, following *Notz and Worster* [2008].

It is noteworthy that the formulation of *Freitag* [1999] for ice permeability was developed for young sea ice (<30 cm), and a more appropriate formula would be the one of *Eicken et al.* [2004] derived from first-year ice at Barrow. However, we chose to compute permeability using the formulation of *Freitag* [1999] for consistency and comparison with previous work [*Notz and Worster*, 2008].

2.6 Stable isotopes of water

We determine δD and δ^{18}O [*Weston*, 1955] in 15 ml aliquots of the melted ice samples (used for the bulk salinity measurements), brine and seawater samples. Stable isotope measurements

were carried out at the Stable Isotope Ratio for Environmental Research Laboratory at the University of Utah using a thermo-chemical elemental analyzer (TCEA) coupled to a Thermo Finnigan Delta Plus XL Isotope Ratio Mass Spectrometer (measured against VSMOW – Vienna Standard Mean Ocean Water) at a precision of 0.03 ‰ for $\delta^{18}O$ and 0.4 ‰ for δD.

2.7 Nutrient and chlorophyll-a

Ice core sections, brine and seawater samples were melted in the dark at 4 °C and filtered through 0.4 µm polycarbonate filters, within 24 hours after ice extraction. Inorganic nutrients were analyzed by colorimetry according to the methods described in *Grasshoff et al.* [1983]. To avoid matrix effect, standards used for calibration were prepared in artificial seawater solutions with salinities similar to those of the samples analyzed. For chlorophyll-a (chl-a) measurements, the ice samples were melted in the dark, in 0.2 µm filtered seawater (1:4 volume ratio) to avoid osmotic stress. We used 10 µm and 0.8 µm polycarbonate filters in a sequence in order to distinguish larger micro-algae species from the smaller ones. Extractions and calculations were made following the procedure of *Arar and Collins* [1997]. We then calculated the standing stock of chl-a, i.e. we integrated the concentrations vertically to obtain the chl-a content per square meter of ice.

2.8 Argon

Argon (Ar) is an inert gas and is therefore not involved in biogeochemical processes. We used the dry-crushing technique as developed for gas measurements in continental ice [*Raynaud et al.*, 1982]. The measurements have been carried out back in Belgium within 15 months after the survey. Each ice core was cut every 5 cm, and 60 g of sample was introduced into a vessel, with 7 stainless steel balls. We evacuated the vessel to 10^{-3} torr, and then fixed it to an ice crusher as described in *Stefels et al.* [2012]. After the crushing at -25 °C, the vessel was

kept at -50 °C in a cold ethanol bath, and was connected to the gas chromatograph equipped with a thermal conductivity detector for concentration analyses [*Skoog et al.*, 1997]. We used Alphagaz^{TM}2 He (Air Liquide – P0252) as carrier-gas and a 22 ml packed column (Mole Sieve 5A 80/100; 5 m x 1/8"). The reproducibility of the analyses was 97.8 %.

The amount of gas collected includes both the gas bubbles in the ice and the dissolved phase within liquid brine. Therefore, we compared the evolution of Ar concentration ([Ar]) in bulk ice to its theoretical solubility in ice at saturation. The latter represents the maximum [Ar] that we may find in the dissolved phase, if no supersaturation exists. It is obtained by calculating the solubility of Ar [*Hamme and Emerson*, 2004] using temperature and salinity in brine and weighting it by the brine volume fraction in the ice. The difference between observed concentration in bulk ice and the theoretical solubility in ice at saturation provides a maximum estimate of the bubble content.

It is noteworthy that the relationship of *Hamme and Emerson* [2004] was established for temperatures between 0 °C and 30 °C and for salinities between 0 and 34.5. We thus assumed in our calculations of Ar solubility that these still hold for the range of temperature and salinity found in our brine samples. This assumption seems reasonable, because we compared our inventory of Ar solubility with an alternative calculation that assumes that temperature and salinity are fixed at 0 °C and 34.5 respectively (the lowest temperature and highest salinity for which Ar solubility is experimentally known [*Hamme and Emerson*, 2004]), and the appropriate brine volume at each depth: the mean difference between both calculations was only 0.059 $\mu mol \cdot L^{-1}$. This result indicates that calculations of Ar solubility are much more sensitive to changes in brine volume fraction than to different assumptions regarding the dependence of solubility on temperature and salinity as expressed by *Hamme and Emerson* [2004].

3. Results

3.1 Physical framework

The stratigraphy of representative cores from each sampling event is shown in Figure 4. The sampling area was highly homogeneous, with similar textures for BRW1 to BRW9: granular ice (~2 cm thick) and columnar ice down to the ice bottom, with a transition layer ("transition ice") with both granular and columnar ice in between (~10 cm thick). From BRW1 to BRW9, the boundary between the transition ice and the columnar ice was particularly bubble-rich (Figure 4b). The bubbles were a few millimetres in diameter. Porous ice with larger bubbles and pores (ca. 2 cm diameter), interleaved with superimposed ice layers [*Haas et al.*, 2001], was observed from 0 cm to 20 cm at BRW10. Maximum snow depth was measured at BRW4 (40 cm) with no snow at BRW10.

Figure 5 shows the evolution of temperature, bulk ice salinity, brine salinity, brine volume fraction and Ra, within the ice cover, interpolated from the 10 sampling events (dots on Figure 5). The evolution of temperature can clearly be divided into 3 stages: (1) A cold stage, from BRW1 to BRW7, where ice temperature decreased from the seawater freezing point at the ice base to colder values near the top; (2) A transition stage (BRW7 to BRW9) where the temperature near the surface increased and the temperature gradient weakened; (3) A warm stage (BRW9 to BRW10) where the temperature profile was nearly isothermal, with a slight temperature increase from the base to the top of the ice.

During the cold stage, all salinity profiles exhibited a typical c-shape, with higher salinities in the top and bottom ice layers compared to those in the ice interior. The bulk ice salinity profiles (Figure 5b) showed a marked transition between BRW7 and BRW8. From BRW8

onward, the surface salinity decreased, particularly at BRW10 where the salinity at the top approached 0.

As brine salinity depends solely on temperature, calculated brine salinity (Figure 5c) is the mirror image of the temperature profile. During the cold stage, brine salinity was higher at the top of the sea ice than at the bottom. Then during the transition stage, the differences between the top and the bottom layers greatly diminished. Brine salinity was closer to seawater salinity (32) for these sampling events. Finally, during the warm stage, brine salinity was lower at the top than at the bottom.

The brine volume fraction (Figure 5d) also showed a sharp shift between BRW7 and BRW8. During the cold stage, only the bottom ice layer had a brine volume fraction above 5 %, considered as a permeability threshold for fluid transport through sea ice, according to *Golden et al.* [1998] and *Pringle et al.* [2009]. The brine volume fractions exceeded 5 % throughout the ice cover from BRW8 onwards. We can make a further distinction among the fully permeable ice cores. During the transition stage (BRW8 and BRW9), the brine volume fraction increased downwards. During the warm stage (BRW10), because of high temperatures and despite the low bulk sea ice salinity, brine volume fraction increased upwards, approaching nearly 30 % at the ice surface.

The Ra (Figure 5e) was always close to 0.5 to 1 at the sea ice bottom. In the ice interior, Ra was always close to 0 except during the transition stage (BRW8 and BRW9) (Ra up to 8). Although Ra was higher than average at these sampling events, Ra never exceeded the critical convection threshold value of 10. This is rather surprising because during the transition stage, a high fluid permeability (brine volume fraction above 5 %) was observed and the unstable brine salinity gradient was reduced; these observations suggest potential brine convection and drainage.

3.2 Isotopic composition

3.2.1 Sea ice isotopic composition

Figure 6 shows data on isotopic composition of bulk ice, snow and seawater. Ice δD and $\delta^{18}O$ profiles appear similar. We observe five main common features related to the ice δD and $\delta^{18}O$ depth profiles: (1) 0 cm to 5 cm depth: there appears a wide range with contrasting signatures. Late in the season, δD and $\delta^{18}O$ reached the lowest values (-67.2 ‰ and -8.2 ‰ respectively). (2) 5 cm to 20 cm depth: the values scatter around a mean value of -2.0 ‰ δD and -0.2 ‰ $\delta^{18}O$. (3) 20 cm to 40 cm: there is a transition zone, with local minima at 30 cm (δD = -4.0 ‰ to -10 ‰ and $\delta^{18}O$ = -0.4 ‰ to -1.3 ‰) then rising to maximal observed values at 40 cm (δD = +8.0 ‰ to +2.0 ‰ and $\delta^{18}O$ = +0.8 ‰ to +1.2 ‰). (4) 40 cm to 90 cm: while the earlier sampling events (BRW2 and BRW4) showed a slight decrease of δ values from 40 cm to 90 cm, the later samplings (BRW7, BRW8 and BRW10) showed relatively constant δ values (δD = -1.0 ‰ to +8.0 ‰ and $\delta^{18}O$ = +0.1 ‰ to +1.2 ‰). (5) Bottom section (bottom-most 40 cm): we observe a steeper gradient of decreasing δ values, corresponding to the layer of sharp brine volume increase (Figure 5d).

3.2.2 Brine isotopic composition

We hypothesized that the isotopic composition measured on bulk sea ice is due to the contribution of both brine and pure ice.

$$\delta D_{bulk\ ice} = (V_{brine} \cdot \delta D_{brine}) + (V_{pure\ ice} \cdot \delta D_{pure\ ice}) \quad (2)$$

$\delta D_{pure\ ice}$ only depends on processes occurring during freezing and should not evolve over time. Indeed, solid-state diffusion is not relevant at seasonal timescales and no fractionation occurs in the solid on melting. Any temporal variation of $\delta D_{bulk\ ice}$ is hence due to changes in the relative volume fractions of pure ice and brine ($V_{pure\ ice}$ and V_{brine}) and changes in δD_{brine}. The pure ice volume fraction $V_{pure\ ice}$ and the brine volume fraction V_{brine} can be derived from

temperature and salinity data [Cox and Weeks, 1983; Petrich and Eicken, 2010], yielding δD_{brine} according to:

$$\delta D_{brine} = \frac{\delta D_{bulk\ ice} - (V_{pure\ ice} \cdot \delta D_{pure\ ice})}{V_{brine}} \quad (3)$$

We hypothesized that isotopic variation in the brine (δD_{brine}) is controlled by internal phase changes and brine drainage processes with subsequent infiltration of snow meltwater or replenishment by seawater. Therefore, in an attempt to track the brine dynamics, we reconstructed the evolution of δD_{brine} and compared them to that of δD values of snow and seawater. Similar calculations could be done for $\delta^{18}O$. However, we focused the discussion on δD because the fractionation factor is larger for δD [Weston, 1955], hence changes of δD_{brine} would be more obvious than those of $\delta^{18}O_{brine}$.

The δD_{brine} at BRW7, BRW8 and BRW10 were estimated using equation 3. Because the latest δD_{brine} is only available for BRW4, we used this value to estimate the $\delta D_{pure\ ice}$ at BRW4 ($\delta D_{pure\ ice\ 4}$) and we assumed that it is the same for BRW7, BRW8 and BRW10 at the respective depth levels in the ice. The thickness of BRW4 hence constrained further calculations to a maximum depth of about 1 m. Re-arranging equation 3 for this specific use, we then calculated $\delta D_{brine7,8,10}$ from:

$$\delta D_{brine7,8,10} = \frac{\delta D_{bulk\ ice7,8,10} - (V_{pure\ ice7,8,10} \cdot \delta D_{pure\ ice\ 4})}{V_{brine7,8,10}} \quad (4)$$

The results are plotted in Figure 7, and only for depths below 40 cm depth (given contrasting signature in the top 40 cm – as discussed below). Measured δD_{brine} from sackholes represents an integration of δD_{brine} in the ice above the sackhole depth. The reconstructed δD_{brine} profiles may therefore not be accurate, but their relative temporal trend is still of interest. δD_{brine} profiles increased in homogeneity over time (standard deviations of δD_{brine} at BRW7, BRW8

and BRW10 were 48.0, 14.7 and 11.9 respectively). From BRW7 to BRW8, values approached the seawater level, while they drifted towards lower δD_{brine} between BRW8 and BRW10.

3.3 Nutrients

Bulk ice nutrient concentrations are compared to the dilution curve for seawater at BRW2, typical seawater of the main growth period (Figure 8). Any deviation from the dilution curve can be attributed to biological activity [*Thomas et al.*, 2010]. Nitrate (NO_3^-) and phosphate (PO_4^{3-}) show a similar relationship to salinity, and that relationship appears to differ between the cold stage (BRW2 and BRW7) and the transition and warm stage (BRW8 and BRW10). During the cold stage, NO_3^- and PO_4^{3-} first scatter around the dilution curve (BRW2) and then increase slightly above the dilution curve (BRW7). With the transition stage, data points fall below the dilution curves. Ammonium (NH_4^+) concentrations in bulk ice were always higher than the dilution curve with a maximum at BRW7.

Nutrients in snow, brine and seawater were standardized at a salinity of 5 for comparison. All nutrients in snow were above the dilution curve. While [PO_4^{3-}] and [NH_4^+] in snow were similar to those in bulk ice, [NO_3^-] in snow exceeded largely concentration observed in bulk ice. In brine, [NO_3^-] and [PO_4^{3-}] were both close to concentrations observed in bulk ice at BRW7, but then decreased at BRW8. As the nutrient concentrations in the brine dropped, we observed a corresponding rise in their concentration within the underlying seawater. The values in seawater then remained stable.

[NH_4^+] did not follow the trend observed for [NO_3^-] and [PO_4^{3-}]. At BRW7, when [NO_3^-] and [PO_4^{3-}] in brine and seawater were close to their concentrations in bulk ice, [NH_4^+] in brine and seawater were well below their concentrations in bulk ice. Then, while changes were

observed for [NO_3^-] and [PO_4^{3-}] between BRW7 and BRW8, [NH_4^+] remained close to 0 and well below the dilution curve for both BRW7 and BRW8. In contrast, [NH_4^+] in brine increased at BRW10 and was found above the dilution curve, when [NO_3^-] and [PO_4^{3-}] in brine were below the dilution curve and were close to 0.

3.4 Chlorophyll-a

The total chl-a (standing stock) increased from BRW1 (0.3 mg·m^{-2}) to BRW10 (8.3 mg·m^{-2}), with two decreases (BRW4 and BRW8) and subsequent resumption of the trend towards increasing values (Figure 9). Large species were always dominant in the sea ice. Their dominance within sea ice increased with time (Figure 9).

Figure 10 shows chl-a concentration ([chl-a]) in ice in the upper box, and [chl-a] in seawater in the lower box. In both cases, we differentiate two groups of autotrophs based on cell size, 0.8 µm to 10 µm and above 10 µm (Figure 10, black bars and grey bars respectively). The coloured dots are values for algae in the brines or snow. The distribution of [chl-a] in sea ice showed large vertical variability, with as expected the highest concentrations being observed in the bottom-most layers [e.g., *Arrigo et al.*, 2010; *Horner et al.*, 1992]. Prior to BRW7, the [chl-a] in sea ice (generally above 0.5 µg·L^{-1}) was higher than that in seawater (0.1 µg·L^{-1}). By BRW8, we observed a sharp decrease of [chl-a] throughout the ice cover, corresponding to an increase in the seawater (0.5 µg·L^{-1}). The [chl-a] further increased in both sea ice and seawater at BRW9 and BRW10. [chl-a] in brine was always close to 0, except in the permeable layers of BRW7 and BRW9 (Figure 5d).

3.5 Argon

The evolution of Ar concentration ([Ar]) in bulk sea ice (filled dots) is compared to the theoretically determined Ar solubility in sea ice using temperature and salinity in brine

(crosses) and temperature and salinity fixed to 0 °C and 34.5 respectively (empty dots, see material and methods) (Figure 11). [Ar] measured in bulk sea ice integrates both dissolved Ar and Ar content in gas inclusions (gas bubbles) in sea ice. [Ar] scattered around 5 $\mu mol \cdot L_{ice}^{-1}$ and were generally higher than the theoretical solubility values. Maximum [Ar] was ca. 13 $\mu mol \cdot L_{ice}^{-1}$ and was observed at sea ice bottom of BRW7 and at the top of BRW10, within the layer of porous ice interleaved with superimposed ice layers. Maximum supersaturation (measured [Ar] divided by the solubility) for the analyzed sampling events were however observed ca. 12 cm depth and ranged between 2200 % and 3800 %. [Ar] always corresponded to the theoretical solubility value (ca. 3 $\mu mol \cdot L_{ice}^{-1}$) in the bottom layer and at all depths beneath the superimposed ice layers at BRW10. If gas bubble nucleation occurred once dissolved Ar exceeds the theoretical solubility value, the results would suggest that gaseous Ar represented the largest fraction of total Ar in sea ice until BRW8.

4. Discussion

4.1 Physical framework

The predominance of columnar ice throughout the ice column at all sites indicates that sea ice growth occurred in calm conditions [*Weeks*, 2010]. The homogeneity of the ice stratigraphy and ice texture between samples also supports the conjecture that most trends in the observed variables result from temporal rather than spatial variability. The temporal evolution of sea ice thickness, temperature and salinity gradients are consistent with those from previous studies in the same area [e.g., *Backstrom and Eicken*, 2006; *Lee et al.*, 2008; *Pringle et al.*, 2007].

Evolution of temperature and salinity (and derived brine volume fraction and brine salinity) can be divided into 3 main stages: (1) A cold stage (BRW1 to BRW7) with ice temperature decreasing from the bottom to the top of the sea ice cover, and the salinity characterized by a

C-shape profile; (2) a transition stage (from BRW7 to BRW9) with ice temperature evolving towards isothermal brine volume fractions of 5 % and surface brine salinity starting to decease and (3) a warm stage (BRW9 to BRW10) with ice nearly isothermal, brine volume maximal at the surface with temperature approaching 0 °C, bulk ice salinity approaching 0 and brine salinity converging towards seawater salinity in the lower half of the ice cover.

During the cold stage, Ra in the ice interior was close to 0. The brine volume fraction was below 5 %, except in the bottom ice layer. The lack of pore connectivity within the brine network [*Golden et al.*, 2007; *Pringle et al.*, 2009] prevented brine percolation despite unstable brine density gradients, by maintaining low permeabilities which in turn kept Ra close to 0. At the other extreme, during the warm stage, brine volume fraction was well above 5%. However, convection was not possible because the brine salinity decreased upwards (Figure 5c); the brine system was stratified. Ra was therefore also close to 0. Between the cold and the warm stage, we have identified a transition stage where brine salinity gradient was unstable and where brine volume fractions exceeded 5 % throughout the ice cover. The brine network was hence expected to be sufficiently connected for sea ice permeability to increase to levels that allow for vertical brine mixing. At this time, Ra had increased, reflecting more favorable conditions for convection to occur.

Ra in this study never exceeded 10, neither in sea ice bottom layer as in the experimental study of *Notz and Worster* [2008], nor in the ice interior during the transition stage despite the favorable conditions for convection to occur. We suggest that ice-core based derivations (from core salinity and temperature data) underestimate Ra, and that convection may occur for apparent values of Ra less than 10. First, Ra is a function of brine salinity and effective ice permeability (Equation 1). Salt loss by drainage during ice core extraction may have led to an underestimation of sea ice salinity, particularly near the ice bottom where others [e.g., *Notz et*

al., 2005] have reported salinity to be underestimated by 1 to 5 and sometimes greater than 10. Such errors in ice salinity lead to an underestimation in Ra in the range of 2 to 10. Second, sampling only gives a snapshot of variables that are highly time dependent. For instance, super-critical Ra values which take several weeks to build-up over the full depth of the ice vanish within one or two days due to convection [*Vancoppenolle et al.*, 2010]. For the two reasons outlined above, detecting critical Ra values from ice core data is inherently challenging. However, we believe that Ra change with depth and with time may provide insight into whether or not conditions are becoming more favorable for convection. In our case, this would more likely occur in the bottom ice layer from the cold stage to the transition stage, and in the ice interior during the transition stage (Figure 5e). These findings are consistent with those of *Pringle et al.* [2007]. The authors have indeed characterized two types of convective events based on thermal conductivity measurements: The ones occurring near the base of the ice during winter and those occurring further up in the ice interior, late in the season.

The three stages in the evolution of temperature and salinity (and derived brine salinity and brine volume fraction) thus correspond to three stages in sea-ice brine dynamics. (1) The cold stage was associated with sea-ice bottom-layer convection; there is no convection in the ice interior because of the low permeability. (2) The transition stage was associated with full-depth convection because sea ice permeability and brine salinity gradients were both favourable for convection to occur. (3) The warm stage was associated with a complete lack of convection due to brine stratification. The evolution of biogeochemical compounds discussed in the following section supports the characterisation of brine dynamics.

4.2 Isotopic composition

4.2.1 Sea ice isotopic composition

In general, the $\delta^{18}O$ isotopic range in the ice is similar to data collected at the Barrow site in 2006-2008 (-1.5 ‰ to 1 ‰; seaice.alaska.edu/gi/data). However, rather than a regular increase of the isotopic composition from the surface to the bottom of sea ice, as generally observed in landfast sea ice [e.g., *Eicken*, 1998], our data show a large variation of the isotopic composition at the surface and a sharp transition ca. 20 cm to 40 cm. Three processes control the δ profiles: the freezing rate, the isotopic signal of the seawater from which sea ice originated and potential post-genetic disturbance [*Eicken*, 1998; *Souchez and Jouzel*, 1984]. The latter is generally associated with rafting, seawater seepage or (snow) meltwater seepage, and hence implies changes in salinity.

The minimum value observed at the surface of BRW10 is explained by post-genetic modification in the form of admixture of snow meltwater. Indeed, the bulk isotopic signature at the ice surface was close to that observed in snow (Figure 6), and the fact that ice salinity approached 0 (Figure 5b) suggests snow melting and flushing [*Eicken et al.*, 2004; *Vancoppenolle et al.*, 2007]. Moreover, the observation of superimposed ice formation (Figure 4a) implies seepage of snow meltwater and subsequent freezing on contact with sea ice [*Haas et al.*, 2001].

A sharp transition in $\delta^{18}O$ and δD at ca. 20 cm to 40 cm was found in all cores analyzed for isotopic composition. The thin sections showed no visible disruption in the core stratigraphy or crystal texture at this depth level, suggesting undisturbed growth and the absence of post-genetic disturbance. As sea ice thickens, the freezing rate declines, which would result in a gradual increase of the respective δ values [*Eicken*, 1998; *Souchez and Jouzel*, 1984]. However, at the Barrow site, changes in the sea ice growth rate at depths below 40 cm were

small such that any signal due to changing growth rate was likely overwhelmed by changes in the composition of the parent water mass.

Changes in the isotopic signatures of the parent water can be explained by freshwater input or changes in isotopic composition due to advection of different water masses. There are no major rivers in the vicinity of the site, but discharge from Elson Lagoon just east of the sampling site may explain lower isotopic signatures in the early growth season (top 20 cm). *Johnson* [1989] and *Weingartner et al.* [2005] report that Barrow coastal waters are impacted by the combined actions of (1) mean seawater flow coming from the Bering Strait and the Herald Valley forced by the sea-level slope, (2) prevailing south-westwards winds and (3) growth of the sea ice cover. The mean current opposes the prevailing winds and, depending on the balance of both factors, Barrow coastal water is influenced by south-westward or north-eastward flows [*Weingartner et al.*, 2005]. We suggest that at the onset of ice growth, water with lower $\delta^{18}O$ (-2 ‰ to -8 ‰) advected in response to wind forcing from the Beaufort Sea [*Yamamoto-Kawai et al.*, 2010]. Moreover, remnant surface water containing higher proportions of surface runoff may still have prevailed as well. Once the sea ice reached a thickness of 20 cm to 30 cm, wind influence dropped and flow to the Northeast prevails, raising the $\delta^{18}O$ (-1 ‰ to -2 ‰) [*Yamamoto-Kawai et al.*, 2010]. In addition, increased mixing of inshore waters due to ice formation and brine discharge may have contributed to diluting the signatures of isotopically light surface water layers impacted by surface runoff.

4.2.2 Brine isotopic composition

At BRW8, brine volume fraction and Ra increased sharply (Figure 5d, e), suggesting that convection within the sea ice brine system may have been active. The fact that the δD_{brine} homogenised towards seawater values at BRW8 (Figure 7) supports the prospect of mixing between the sea ice brine system and seawater, with partial brine replacement by seawater.

This observation supports the occurrence of convection, particularly at BRW9 where higher Ra values were observed (Figure 5e). The later drift of δD_{brine} towards lower values between BRW8 and BRW10 further supports that snow melting was generalized, with active flushing during the warm stage.

Finally, δD_{brine} in the bottom 10 cm to 20 cm was always at seawater value. The steeper drop of $\delta D_{bulk\ ice}$ through the bottom 10 cm to 20 cm at nearly all the sampling events coincided with the increase in brine volume fraction in sea ice bottom (Figure 6). Higher brine volume fraction means a larger seawater contribution, which drives down the $\delta D_{bulk\ ice}$.

4.3 Nutrients

Our data range is consistent with those of *Krembs et al.* [2002] and *Lee et al.* [2008] obtained in Barrow landfast ice as well. The comparison of individual data points with the dilution curve (Figure 8) provides insight into the balance between physical and biological processes active in the brine. $[NO_3^-]$, $[PO_4^{3-}]$ at the beginning of the cold stage (BRW2) align along the dilution curve when plotted against the salinity, indicating that physical processes (nutrient incorporation in sea ice and subsequent transport within the brine system) dominate over biological nutrient turnover. In contrast, nutrient concentrations at the end of the cold stage (BRW7) point to dominant heterotrophic processes with recycling and accumulation of by-products from the activity of bacterial metabolism (dots above the dilution curve). However, from the transition stage to the warm stage (BRW8, BRW10), $[NO_3^-]$ and $[PO_4^{3-}]$ decreased which we attribute to convection and biological consumption as outlined below.

An incursion of seawater into the brine network at BRW8 would have resulted in a slight lowering of nutrient concentrations. We explore this possibility through the use of theoretical nutrient concentrations ($[NO_3^-]$ and $[PO_4^{3-}]$) in bulk sea ice. Our theoretical estimate assumes

that the nutrient concentrations at the sea ice/seawater interface at BRW7 (5.3 µmol·L^{-1} and 1.0 µmol·L^{-1} for NO_3^- and PO_4^{3-} respectively) fills between 5 % and 30 % of bulk ice throughout the sea ice vertical profile at BRW8. The percentages were defined given the brine volume fractions at BRW8 (Figure 5). In the estimate we neglect potential biological consumption, which we feel is valid given the low [chl-a] measured at BRW8 (Figure 10). Resulting concentrations in ice range from 0.3 µmol·L^{-1} to 1.6 µmol·L^{-1} for NO_3^- and 0.05 µmol·L^{-1} to 0.3 µmol·L^{-1} for PO_4^{3-}. These values cover the measured range of sea ice nutrient content at BRW8 (Figure 8), supporting our hypothesis that seawater had replaced the brine. It is noteworthy that brine drainage induced fewer changes in nutrients than in δD_{brine}. This is because nutrient concentrations in seawater were already close to those in brine, while isotopic fractionation led to larger difference between δD in brine and δD in seawater.

At BRW10, [NO_3^-] and [PO_4^{3-}] further decreased in bulk ice, brine and surface seawater. The decrease in the bulk of the ice indicates internal nutrient consumption, with limited resupply from seawater. Convection processes at that time were indeed unlikely (see physical framework); hence nutrient resupply from seawater was limited. We believe that nutrient supply at this time was mainly through remineralisation [*Lee et al.*, 2008] and diffusion from seawater [*Vancoppenolle et al.*, 2010]. Nutrient consumption may have supported the increase in algal biomass from BRW8 to BRW10 (Figure 9 and Figure 10) in bulk ice and seawater.

The temporal evolution of [NH_4^+] differed from those of [NO_3^-] and [PO_4^{3-}] but parallels those observed in previous studies [e.g., *Lee et al.*, 2008]. At first sight, the evolution of [NH_4^+] reflects the balance between bacterial degradation and the uptake by phytoplankton [*Becquevort et al.*, 2009; *Lee et al.*, 2008]. However, the results further showed that bulk ice had conspicuously higher [NH_4^+] than brine (not observed for [NO_3^-] and [PO_4^{3-}]). This phenomenon has also been reported in *Becquevort et al.* [2009] for Antarctic sea ice. Two

processes that can lead specifically to higher [NH_4^+] in bulk ice than in brines: NH_4^+ incorporation in the pure ice matrix and NH_4^+ adsorption on exopolymer substances (EPS) [e.g., *Gradinger and Ikävalko*, 1998; *Krembs et al.*, 2002]. First, NH_4^+ is indeed one of the few chemical compounds that can be incorporated into the ice crystal through substitution [*Weeks*, 2010]. If this occurred, ice melting during the warm stage would transfer NH_4^+ from the ice matrix to the brine and foster sea ice algae growth. Second, the acidic nature of EPS favours cation adsorption [*Hart et al.*, 2001]. If NH_4^+ adhered to the walls of brine inclusions, just like chl-a during the cold stage (see next section), its drainage into brine sackholes would be unlikely. We believe that this second process was predominant at BRW7, since [NH_4^+] in bulk ice increased significantly but NH_4^+ production in the pure ice matrix is unlikely.

Nutrient concentrations in snow were above the dilution curve at BRW7 (Figure 8). In particular, [NO_3^-] in snow was well above the respective concentration in bulk ice. This indicates that NO_3^- in snow was due to atmospheric supply rather than brine expulsion. Atmospheric supply of NO_3^- through snow deposit has also been observed in the Baltic Sea, where it likely affects the biological productivity in sea ice and in under-ice water through gravity drainage. [*Granskog et al.*, 2003].

4.4 Chlorophyll-a

The proportion of large phototrophic organisms increased within sea ice from January through June (Figure 9), as found in previous studies at the site [e.g., *Horner and Schrader*, 1982; *Krembs et al.*, 2001]. Also in agreement with previous findings [*Gradinger et al.*, 1991; *Juhl and Krembs*, 2010], our study suggests an impact of snow cover on algal biomass in sea ice. Although total [chl-a] increased from BRW1 (0.3 $mg \cdot m^{-2}$) to BRW10 (8.3 $mg \cdot m^{-2}$) (Figure 10), this range is well below biomass levels found in earlier studies in the same area (e.g., 27 $mg \cdot m^{-2}$) in 2003 [*Lee et al.*, 2008]). This may be explained in part by the comparatively deep

snow cover in 2009. For comparison, whereas the snow depth was only between 10 cm and 15 cm in 2003 [*Jin et al.*, 2006], it ranged between 13 cm and 39 cm in the present study. Heavier snow cover attenuates light and hence lowers photosynthetic activity [*Gradinger et al.*, 1991; *Juhl and Krembs*, 2010; *Mundy et al.*, 2005].

While snow cover may have impacted the overall range of total [chl-a] in sea ice, gravity and convective drainage impacted total [chl-a] in specific ice cores. The gradual increase of total [chl-a] over the study period was punctuated by two apparent reductions in biomass. At BRW4, the drop in [chl-a] could be related to spatial variability or to the loss of bottom biomass by gravity drainage during sample extraction. Since micro-organisms were mainly concentrated near the bottom (Figure 10), loss by gravity drainage could have drastically impacted the total [chl-a]. At BRW8, the decrease of [chl-a] was not limited to the bottom layers, but occurred throughout the entire ice thickness (Figure 10). A twin ice core has been melted and variation in total [chl-a] did not exceed 5 %. Moreover, since the decrease of [chl-a] was coupled to the increases of $Ra_{Freitag}$ and of [chl-a] at the ice-seawater interface, we interpret the [chl-a] decrease at BRW8 as the result of convective overturning, rather than spatial variability.

Linking [chl-a] decreases in sea ice to convective processes implies that micro-algae could be drained from sea ice. However, it has been shown that micro-algae produce exopolymer substances (EPS) that favour their attachment to the walls of brine inclusions [e.g., *Gradinger and Ikävalko*, 1998; *Krembs et al.*, 2002]. Low [chl-a] in brine collected from sackholes supports this suggestion. Figure 12 describes the relationship between the total chl-a and the brine volume fraction and may help resolve this apparent contradiction. There is a positive correlation between both parameters in BRW1 to BRW7, suggesting that larger brine volume fractions, characteristic of the bottom layers, favours higher standing stocks. Possible

explanations of this observation include: (1) higher nutrient supply, (2) more space within which algal communities can develop high biomass or (3) high salinities (typically above 100, dark grey dots) and low temperatures inhibit algae growth at small brine volumes. The transition to brine volume fractions above 5 % (increasing the permeability of the internal layers above the percolation threshold), combined with convective processes associated with the increase of $Ra_{Freitag}$ result in a complete obliteration of the chl-a and brine volume relationship. This suggests that these processes can overwhelm the EPS-binding mechanism, leading to biomass drainage and removal, increasing their concentration at the ice-seawater interface. *Krembs et al.* [2001] and *Gradinger et al.* [1991] have also suggested that sea ice permeability and brine drainage could impact ice algal build-up.

Our study further recorded rapid chl-a resumption, despite low nutrient concentrations (Figure 8 and Figure 9). This contrasts with the results of *Jin et al.* [2006], suggesting that convective process increases nutrient supply supporting algal growth at Barrow at the same period. Total chl-a was 1.5 mg chl-a$\cdot m^{-2}$ at BRW8, but 4.0 mg chl-a$\cdot m^{-2}$ at BRW9, 4 days later. According to *Arrigo et al.* [2010], carbon (C):chl-a ratio is between 20 and 40. We applied the ratio of 30 to BRW8 and BRW9 and got 45 mg C$\cdot m^{-2}$ and 120 mg C$\cdot m^{-2}$ respectively. The inferred carbon uptake rate is 19 mg C$\cdot m^{-2}\cdot d^{-1}$, which is consistent with that reported by *Lee et al.* [2008] at Barrow (16 mg C$\cdot m^{-2}\cdot d^{-1}$ the 28th of April). The authors have also noticed algae growth despite of nutrient depletion; this was associated to the increase of carbon-allocation into algal lipids. In addition, the increase in the proportion of large species throughout the annual cycle may suggest that these species were more adapted to large brine volumes and low nutrient conditions.

4.5 Argon

Our data range (0.7 µmol·L_{ice}^{-1} to 13.0 µmol·L_{ice}^{-1}) is consistent with the results of *Matsuo and Miyake* [1966]. Ar profiles are different from those of the other analysed inert compounds (salt via salinity and isotopes). First, the increase in [Ar] at the base of the transition zone between granular and columnar ice was not observed in all the profiles of the other compounds. Second, while chl-a and nutrients decreased with convective brine drainage during the transition stage (BRW8), Ar further accumulated in sea ice. Third, when chl-a increased again during the warm stage (BRW10), [Ar] dropped to ice solubility values in most of the profile. We suggest that bubble nucleation and migration were the main drivers for the observed differences, because in contrast to the other compounds Ar may be present in the form of gas bubbles. We first discuss how gas bubbles could form in sea ice and then how their formation led to the observed Ar profiles.

Within a closed sea ice system, the ratio between the dissolved and the bubble state of Ar depends on the gas solubility in the liquid. [Ar] in the bottom ice layer was always at the solubility limit, suggesting that Ar incorporation at the ice-seawater interface occurred close to the solubility value. Once incorporated into the ice cover, Ar is exposed to a decrease in temperature and an increase in brine salinity. Decreasing temperature increases Ar solubility but the salinity effect dominates so that Ar solubility in brine (and therefore in bulk ice) decreased after incorporation [*Hamme and Emerson*, 2004]. As a consequence, a portion of the dissolved gas is forced out of solution and into bubble. Within a closed system however, the total amount of Ar per unit mass of ice (dissolved + bubble state) should remain constant. We therefore expect a more or less constant value of 3 µmol·L_{ice}^{-1} as near the sea ice bottom. The increasing deviation of the measured [Ar] from the solubility limit moving from the ice bottom to the surface (at BRW2 and BRW4) therefore requires the addition of Ar.

Bubble nucleation due to solubility decrease in an open system (i.e. connected to the seawater) could explain the rise in [Ar] in bulk ice. First, on nucleation bubbles may rise due to their buoyancy [*Frank et al.*, 2007], until they are blocked from further migration by reductions in ice permeability. Second, in an open system, brine replacement by seawater through convective processes will increase the Ar content in sea ice given at saturation in brine is lower than [Ar] at saturation in seawater. Ar solubility in the "new" brine would be subject to a lower temperature and higher salinity, resulting in the formation of new bubbles through the lowering of brine solubility for Ar. Repeated convective events may then be effective at raising bulk Ar concentration in sea ice (Figure 13).

Although further laboratory experiments are needed to assess the suggested scenario, we cannot exclude bubble formation within sea ice. Indeed, the highest Ar supersaturations for the presented sampling events ranged between 2200 % and 3800 %. This range is consistent with the supersaturation level at which *Killawee et al.* [1998] observed nitrogen bubble formation. Moreover, the highest Ar supersaturations were found at the base of the transition level where thin sections showed high bubble content. Furthermore, first results of model simulations indicate at least 50 % underestimation of the Ar content within sea ice if the process of bubble formation is not taken into account [*Moreau et al.*, submitted].

Bubble nucleation due to the decrease of solubility contributed significantly to bubble accumulation within sea ice in winter, because of the strong temperature (hence brine salinity) gradient between the top and the bottom of the permeable layers. Since this gradient weakened as the sea ice thickened and its surface temperature increased (Figure 5). Other processes need to be considered to explain the additional incorporation of Ar at the sea ice bottom of BRW7 and BRW8.

Bubble nucleation can also occur at low supersaturation [*Jones et al.*, 1999]. The requirements are (1) pre-existing gas cavities in the surface of the substrate and (2) local fluctuations in the gas-supersaturated liquid. These requirements were satisfied at BRW8. The gas cavities were gas inclusions trapped within brine-filled pores and the local fluctuations were provided by the full-depth convection events. Hence, in addition to solubility-driven bubble nucleation, gas may further accumulate in sea ice through convection-driven bubble nucleation. Further, heterogeneous nucleation may also favour bubble nucleation [*Jones et al.*, 1999] at the ice base with a large content of hydrophobic composites. Since the sea ice bottom at BRW7 was characterized by one of the highest chl-a contents (i.e. potentially high algal biomass) in the dataset, and since algae can synthesize hydrophobic composites [*Underwood et al.*, 2010], the high [Ar] observed at the sea ice bottom of BRW7 may be related to the presence of hydrophobic composites. Further laboratory experiments are however needed for assessing these conjectures.

Our study further suggests that the permeability threshold for gaseous Ar transport in sea ice could be different from that for brine. Indeed, brine volume fractions exceeded 5 % at BRW8 and BRW10 (Figure 5d). If Ar behaved as brine, sea ice would be permeable for Ar at these porosities. However, accumulation of Ar below 85 cm at BRW8 indicates that Ar was trapped by impermeable sea ice. In contrast, [Ar] at solubility values (beneath the superimposed ice layers) at BRW10 indicates that a significant amount of bubbles escaped. The comparison of the layers above 85 cm between both sampling events reveals that the brine volume fraction in these layers was below 7.5 % at BRW8, but above 10 % at BRW10. Therefore, the critical porosity threshold for upward transport of Ar (and possibly other gases as bubbles) in our study may be between 7.5 % and 10 % of brine volume fraction. These brine volume fractions are associated to a temperature of -3.5 °C and -2.5 °C respectively for a bulk ice salinity of 5. The present study thus moderates the statement of *Gosink et al.* [1976] suggesting gas

migration through sea ice for temperatures above -10 °C. It is however in agreement with the findings of *Loose et al.* [2010] showing gas diffusion through young sea ice (< 15 cm thick) between 6.1 % to 7.9 % of brine volume fraction.

If Ar bubbles escape from sea ice for brine volumes approaching 10 %, such escape should have occurred between BRW9 and BRW10 (Figure 5d) and have led to a decrease of [Ar]. Finding [Ar] up to 13 $\mu mol \cdot L_{ice}^{-1}$ at the ice surface of BRW10 is then surprising. There are three potential explanations for this observation: (1) The [Ar] originated from a direct input of atmospheric air. Since sea-ice freeboard was positive, atmospheric air could have filled the ice pores, following brine drainage, and increased [Ar]. (2) The [Ar] originated from bubble upward migration. Indeed, superimposed ice layers were observed at BRW10, and these could impede gas exchange between sea ice and the atmosphere [*Tison et al.*, 2008]. Providing that superimposed ice layers were formed between BRW9 and BRW10 and that bubble upward migration was slow, superimposed ice layers could have blocked the bubbles rising up throughout the brine network. (3) The [Ar] was related to superimposed ice formation itself, as a result of snow melt with subsequent rapid freezing at the ice interface. This explanation is supported by the following statements: First, the observed high [Ar] was found within the superimposed ice layers but not underneath, which would have been the case if it was due to bubble upward migration. Second, the measured concentration is equivalent to 0.29 ml $Ar \cdot L_{ice}^{-1}$ in STP, which is similar to that obtained from instant freezing of seawater (0.23 ml $Ar \cdot L_{ice}^{-1}$, assuming 1 % of Ar in total gas content) [*Matsuo and Miyake*, 1966]. Third, the measured concentration is consistent with the solubility of snow and ice meltwater. Indeed, hypothesizing equilibrium between meltwater and the atmosphere and taking into account the bulk salinity of the ice surface (0 cm to 5 cm), which was 0.2, we computed the solubility of Ar at 0°C [*Hamme and Emerson*, 2004] and found 22 $\mu mol \cdot L^{-1}$. The measured concentration (13 $\mu mol\ Ar \cdot L_{ice}^{-1}$) is slightly lower than the computed solubility; this is likely due to the

matrix of pure ice (meltwater only filled pores within the pure ice matrix). Therefore, during the warm stage, despite large brine volume fraction, gas accumulation in sea ice seems possible through superimposed ice formation.

5 Conclusion and perspectives

The present study focuses on the physical properties of landfast sea ice, and their impacts on brine dynamics and ice-ocean-atmospheric exchanges of biogeochemical compounds, during an annual cycle of ice growth and decay (from January through June 2009) at Barrow (Alaska). The main findings are summarized in . We have identified three main stages in the evolution of physical properties (temperature, salinity, brine salinity and brine volume fraction, Ra): a cold stage (BRW1 to BRW7), a transition stage (BRW7 to BRW8) and a warm stage (BRW9 to BRW10). These stages corresponded to three stages in sea-ice permeability and brine dynamics: (1) The cold stage was associated with low permeability in the ice interior, and sea-ice bottom-layer convection; (2) The transition stage was associated with full-depth convection due to the combined effect of permeable ice cover and unstable brine density profile. (3) The warm stage was associated with a complete lack of convection, despite permeable ice cover, due to brine stratification.

Ra was used qualitatively because detecting critical Ra values from ice core data appears to be challenging. Non-destructive, in situ measurements of temperature and bulk salinity (the latter through approaches such as those outlined by *Notz et al.* [2005] or *Backstrom and Eicken* [2006]) can help address this issue. Similarly, temperature traces from time series collected by thermistor arrays may also provide evidence for the onset of convection [*Pringle et al.*, 2007].

The analysed biogeochemical compounds showed distinct behaviour during each of the brine dynamic stages. During the cold stage, the temperature gradient was steep with an effectively

impermeable ice interior and a highly permeable sea-ice bottom-layer. Within the impermeable layer, concentrations of the biogeochemical compounds at the beginning of the cold stage depend strongly on the conditions of sea ice formation and the dominance of physical controls. δD and $\delta^{18}O$ suggest regional changes in water mass properties; nutrient distribution along the dilution curve indicates that physical processes dominate over biological turnover. Chl-a concentrations that correlate well with brine volume fractions suggest that the size of brine inclusions may constrain the distribution of micro-organisms (through the associated temperature, brine salinity and nutrient supply). Ar accumulation within the ice is related to changes in gas solubility and subsequent bubble formation at incorporation. At the end of the cold stage, biological control of the biogeochemical compounds increased: total chl-a increased, and nutrients accumulated in the ice interior due to remineralisation. Such an accumulation confirms that the ice interior was impermeable with a lack of exchange between the ice interior and the under-ice water. In contrast to the impermeable ice interior, convection occurred throughout the whole cold stage within the permeable sea-ice bottom-layer. This ensured nutrient supply and contributed to the high [chl-a] observed near the sea ice bottom.

During the transition stage, brine volume fractions increased throughout the ice cover. This, in combination with the unstable brine salinity gradient, favoured full-depth convection, which then impacted all the biogeochemical compounds. Dissolved compounds reflect brine drainage with partial seawater replenishment: δD_{brine} approached seawater values; NO_3^- and PO_4^- returned to values set by the dilution curve. The solid fraction (chl-a) was also flushed out of the ice. This seeding of nutrients and organic matter likely boosts micro-organism growth in the under-ice water, where concomitant chl-a increase was indeed observed. *Arrigo et al.* [2012] have also reported such an under-ice phytoplankton growth in the Chukchi Sea northeast of Barrow. While both dissolved (isotopes and nutrients) and solid (chl-a) fractions

were flushed from the ice, chl-a showed a rapid resumption. Sharp changes in brine volume fraction and in nutrient concentrations, associated with the transition stage, should promote changes in the ice algal community. As a potential consequence, the proportion of larger micro-organisms within the ice was observed to increase during the transition stage. In contrast to the other compounds, Ar further accumulated in sea ice. We relate this behaviour to its presence in the gaseous phase, and suggest that the formation of bubbles (through convection processes and heterogeneous nucleation) and the subsequent rise due to buoyancy promote Ar accumulation within the ice. Therefore, in contrast to the cold stage, where sea ice interactions with seawater are limited to the bottom layers, during the transition stage such interactions take place throughout the ice column.

Finally, during the warm stage, the brine within the ice column was well stratified, precluding convection. Isotopes indicated downward percolation of snow meltwater into the ice. Nutrient concentrations further decreased since consumption outweighed supply, sustaining the increase of chl-a standing stock through the melt season, with potential contributions of NO_3^- from snow melt and NH_4^+ from ice melt. These observations need to be properly simulated by models of sea ice primary production that rely on a tight link between nutrient supply and ice algal growth. In contrast to the two other stages, interactions between sea ice and seawater are more limited during the warm stage, which is characterized mainly by diffusive rather than convective transport. At the same time, exchange between the ice cover and the atmosphere is more intense. Thus, Ar dropped to the solubility value during this warm stage, suggesting the release of the bubble content to the atmosphere. We estimate that the threshold for significant Ar bubble migration in the brine system is at brine volume fractions of between 7.5 % and 10 %. Our study therefore shows that gases can accumulate in sea ice and persist longer than what would be expected based on brine migration behaviour. This finding has potential

implications for the biological impact of the dynamics of climate-active gases like CO_2 [*Delille et al.*, 2007] and CH_4 [*Shakhova et al.*, 2010] that are incorporated into sea ice.

Acknowledgements

The authors would like to thank Dr. C. Petrich and the sea ice group of the Geophysical Institute of the University of Alaska Fairbanks for installing and maintaining the sea ice mass balance buoy. We are indebted to the Barrow Arctic Science Consortium and the North Slope Borough for their logistical support. We thank Dr. L. Chou and S. El Amri for their efficient help in laboratory work. We gratefully acknowledge the helpful comments and suggestions of the four anonymous reviewers. This research was supported by the F.R.S-FNRS (contract 2.4584.09), the National Science Foundation (project OPP-0632398 (SIZONet)), the University of Alaska Fairbanks and the Belgian Science Policy (contract SD/CA/03A), the NCE ArcticNet and National Science and Engineering Research Council (NSERC). NXG and FB got a PhD grant from F.R.S.-FRIA. JZ is a research fellow of F.R.S.-FNRS, BD is a research associate of F.R.S.-FNRS. This is MARE contribution no. XXX.

References

Arar, E. J., and G. B. Collins (1997), In vitro Determination of Chlorophyll a and Pheophytin a in Marine and Freshwater Algae by Fluorescence (Method 445.0)*Rep.*, National Exposure Research Laboratory - U.S. Environmental Protection Agency, Ohio.

Arrigo, K. R., T. Mock, and M. P. Lizotte (2010), Primary Producers and Sea Ice, in *Sea ice*, edited by D. N. Thomas and G. S. Dieckmann, pp. 283-325, Blackwell Publishing Ltd, UK.

Arrigo, K. R., et al. (2012), Massive Phytoplankton Blooms Under Arctic Sea Ice, *336*(6087).

Backstrom, L. G. E., and H. Eicken (2006), Capacitance probe measurements of brine volume and bulk salinity in first-year sea ice, *Cold Regions Science and Technology*, *46*, 167-180.

Becquevort, S., I. Dumont, J. L. Tison, D. Lannuzel, M. L. Sauvee, L. Chou, and V. Schoemann (2009), Biogeochemistry and microbial community composition in sea ice and underlying seawater off East Antarctica during early spring, *Polar Biol.*, *32*(6), 879-895.

Comiso, J. C. (2010), Variability and Trends of the Global Sea Ice Cover, in *Sea ice*, edited by D. N. Thomas and G. S. Dieckmann, pp. 205-246, Blackwell Publishing Ltd, UK.

Cox, G. F. N., and W. F. Weeks (1983), Equations for determining the gas and brine volumes in sea-ice samples, *J Glaciol*, *29*(102), 306-316.

Delille, B., B. Jourdain, A. V. Borges, J.-L. Tison, and D. Delille (2007), Biogas (CO2, O2, dimethylsulfide) dynamics in spring Antarctic fast ice, *Limnol Oceanogr*, *52*(4), 1367-1379.

Dieckmann, G. S., and H. H. Hellmer (2010), The importance of sea ice: An overview in *Sea ice*, edited by D. N. Thomas and G. S. Dieckmann, pp. 1-22, Blackwell Publishing Ltd, UK.

Druckenmiller, M. L., H. Eicken, D. J. Pringle, C. C. Williams, and M. A. Johnson (2009), Towards an integrated coastal sea-ice observatory: System components and a case study at Barrow, Alaska, *Cold Regions Science and Technology*, *56*, 61-72.

Eicken, H. (1992), The role of sea ice in structuring antarctic ecosystems, *Polar Biol.*, *12*(1), 3-13.

Eicken, H. (1998), Factors determining microstructure, salinity and stable-isotope composition of Antarctic sea ice: Deriving modes and rates of ice growth in the Weddell Sea, in *AGU Antarct. Res. Ser. (Antarctic Sea Ice Physical Processes, Interactions and Variability)*, edited by M. O. Jeffries, pp. 89-122.

Eicken, H., T. C. Grenfell, D. K. Perovich, J. A. Richter-Menge, and K. Frey (2004), Hydraulic controls of summer Arctic pack ice albedo, *Journal of Geophysical Research*, *109*(C08007).

Fofonoff, N. P. (1985), Physical properties of seawater: A new salinity scale and equation of state for seawater, *Journal of Geophysical Research*, *90*(C2), 3332-3342.

Frank, X., N. Dietrich, J. Wu, R. Barraud, and H. Z. Li (2007), Bubble nucleation and growth in fluids, *Chem Eng Sci*, *62*, 7090-7097.

Freitag, J. (1999), Untersuchungen zur Hydrologie des arktischen Meereises-Konsequenzen für den kleinskaligen Stofftransport, *Ber. Polarforsch./Rep. Pol. Res.*, *325*.

Fritsen, C. H., V. I. Lytle, S. F. Ackley, and C. W. Sullivan (1994), Autumn Bloom of Antarctic Pack-Ice Algae, *Science*, *266*(5186), 782-784.

Golden, K. M., S. F. Ackley, and V. I. Lytle (1998), The percolation phase transition in sea ice, *Science*, *282*(5397), 2238-2241.

Golden, K. M., H. Eicken, A. L. Heaton, J. Miner, D. J. Pringle, and J. Zhu (2007), Thermal evolution of permeability and microstructure in sea ice, *Geophys. Res. Lett.*, *34*(L16501).

Gosink, T. A., J. G. Pearson, and J. J. Kelley (1976), Gas movement through sea ice, *Nature*, *263*(September 2), 41-42.

Gradinger, R., and J. Ikävalko (1998), Organism incorporation into newly forming Arctic sea ice in the Greenland Sea, *J Plankton Res*, *20*(5), 871-886

Gradinger, R., M. Spindler, and D. Henschel (1991), Development of Arctic sea-ice organisms under graded snow cover, *Polar Res.*, *10*(1), 295-307.

Granskog, M. A., H. Kaartokallio, and K. Shirasawa (2003), Nutrient status of Baltic Sea ice: Evidence for control by snow-ice formation, ice permeability, and ice algae, *Journal of Geophysical Research*, *108*(3253).

Grasshoff, K., M. Erhard, and K. Kremling (1983), *Methods of seawater analysis*, 2nd ed., Verlag-Chemie.

Haas, C., D. N. Thomas, and J. Bareiss (2001), Surface properties and processes of perennial Antarctic sea ice in summer, *J Glaciol*, *47*(159).

Hamme, R. C., and S. R. Emerson (2004), The solubility of neon, nitrogen and argon in distilled water and seawater, *Deep-Sea Research I - Oceanographic Research Papers*, *51*(11), 1517-1528.

Hart, T. D., J. M. Lynch, and A. H. L. Chamberlain (2001), Anion exclusion in microbial and soil polysaccharides, *Biol Fertil Soil*, *34*, 201–209.

Horner, R. A., and G. C. Schrader (1982), Relative contributions of ice algae, phytoplankton and benthic microalgae to primary production in nearshore regions of the Beaufort Sea, *Arctic*, *35*, 485-503.

Horner, R. A., S. F. Ackley, G. S. Dieckmann, B. Gulliksen, T. Hoshiai, L. Legendre, I. A. Melnikov, W. S. Reeburgh, M. Spindler, and C. W. Sullivan (1992), Ecology of sea ice biota. 1. Habitat, Terminology, and methodology *Polar Biol.*, *12*(3-4), 417-427.

Hunke, E. C., D. Notz, A. K. Turner, and M. Vancoppenolle (2011), The multiphase physics of sea ice: a review for model developers, *The Cryosphere*, *5*, 989-1009.

Jin, M., C. J. Deal, J. Wang, K.-H. Shin, N. Tanaka, T. E. Whitledge, S. H. Lee, and R. R. Gradinger (2006), Controls of the landfast ice-ocean ecosystem offshore Barrow, Alaska, *Ann Glaciol*, *44*, 63-72.

Johnson, W. R. (1989), Current response to wind in the Chukchi Sea: A regional coastal upwelling event, *Journal of Geophysical Research*, *94*(C2), 2057-2064.

Jones, S. F., G. M. Evans, and K. P. Galvin (1999), Bubble nucleation from gas cavities - a review, *Advances in Colloid and Interface Science*, *80*, 27-50.

Juhl, A. R., and C. Krembs (2010), Effects of snow removal and algal photoacclimation on growth and export of ice algae, *Polar Biol.*, *33*(8), 1057-1065.

Killawee, J. A., I. J. Fairchild, J. L. Tison, L. Janssens, and R. Lorrain (1998), Segregation of solutes and gases in experimental freezing of dilute solutions: Implications for natural glacial systems, *Geochim Cosmochim Ac*, *62*(23-24), 3637-3655.

Krembs, C., T. Mock, and R. Gradinger (2001), A mesocosm study of physical-biological interactions in artificial sea ice: effects of brine channel surface evolution and brine movement on algal biomass, *Polar Biol.*, *24*(5), 356-364.

Krembs, C., H. Eicken, K. Junge, and J. W. Deming (2002), High concentrations of exopolymeric substances in Arctic winter sea ice: implications for the polar ocean carbon cycle and cryoprotection of diatoms, *Deep-sea Research I*, *49*(12), 2163-2181.

Langway, C. C. (1958), Ice fabrics and the universal stage*Rep.*, U.S. Snow, Ice and Permafrost Research Establishment.

Lannuzel, D., V. Schoemann, J. de Jong, L. Chou, B. Delille, S. Becquevort, and J. L. Tison (2008), Iron study during a time series in the western Weddell pack ice, *Mar Chem*, *108*(1-2), 85-95.

Lee, S. H., T. E. Whitledge, and S. H. Kang (2008), Spring time production of bottom ice algae in the landfast sea ice zone at Barrow, Alaska, *J Exp Mar Biol Ecol*, *367*(2), 204-212.

Lizotte, M. P. (2001), The contributions of sea ice algae to Antarctic marine primary production, *Am Zool*, *41*(1), 57-73.

Loose, B., P. Schlosser, D. Perovich, D. Ringelberg, D. T. Ho, T. Takahashi, J. Richter-Menge, C. M. Reynolds, W. R. Mcgillis, and J. L. Tison (2010), Gas diffusion through columnar laboratory sea ice: implications for mixed-layer ventilation of CO2 in the seasonal ice zone, *Tellus B*, *63*(1), 23-39.

Matsuo, S., and Y. Miyake (1966), Gas composition in ice samples from Antarctica, *Journal of Geophysical Research*, *71*(22), 5235-5241.

Moreau, S., M. Vancoppenolle, J. Zhou, J. L. Tison, B. Delille, and H. Goosse (submitted), Modeling argon dynamics in first-year sea ice, *Ocean Model*.

Mundy, C. J., D. G. Barber, and C. Michel (2005), Variability of thermal, physical and optical properties pertinent to sea ice algae biomass during spring, *J Marine Syst*, *58*, 107-120.

Niedrauer, T. M., and S. Martin (1979), An Experimental Study of Brine Drainage and Convection in Young Sea Ice, *Journal of Geophysical Research*, *84*(C3), 1176-1186.

Notz, D., and M. G. Worster (2008), In situ measurements of the evolution of young sea ice, *Journal of Geophysical Research*, *113*(C3).

Notz, D., and M. G. Worster (2009), Desalination processes of sea ice revisited, *Journal of Geophysical Research*, *114*.

Notz, D., J. S. Wettlaufer, and M. G. Worster (2005), A non-destructive method for measuring the salinity and solid fraction of growing sea ice in situ, *J Glaciol*, *51*(172), 159-166.

Petrich, C., and H. Eicken (2010), Growth, Structure and Properties of Sea Ice, in *Sea ice*, edited by D. N. Thomas and G. S. Dieckmann, pp. 23-77, Blackwell Publishing Ltd, UK.

Pringle, D. J., and M. Ingham (2009), Thermal, Electrical, and hydraulic Properties of Sea Ice, in *Field Techniques for Sea Ice Research*, edited by H. Eicken, R. Gradinger, M. Salganek, K. Shirasawa, D. Perovich and M. Lepparanta, University of Alaska Press, Alaska.

Pringle, D. J., H. Eicken, H. J. Trodahl, and L. G. E. Backstrom (2007), Thermal conductivity of landfast Antarctic and Arctic sea ice, *Journal of Geophysical Research*, *112*(C04017).

Pringle, D. J., J. E. Miner, H. Eicken, and K. M. Golden (2009), Pore space percolation in sea ice single crystals, *Journal of Geophysical Research*, *114*(C12017).

Raynaud, D., R. Delmas, J. M. Ascencio, and M. Legrand (1982), Gas extraction from polar ice cores: a critical issue for studying the evolution of atmospheric CO_2 and ice-sheet surface elevation, *Ann Glaciol*, *3*, 265-268.

Shakhova, N., I. Semiletov, A. Salyuk, V. Yusupov, D. Kosmach, and O. Gustafsson (2010), Extensive Methane Venting to the Atmosphere from Sediments of the East Siberian Arctic Shelf, *Science*, *327*(5970), 1246-1250.

Skoog, D. A., D. M. West, and F. J. Holler (1997), *Chimie analytique*, De Boeck Université, Paris, Bruxelles.

Smith, W. O., and D. M. Nelson (1986), Importance of Ice Edge Phytoplankton Production in the Southern Ocean, *BioScience*, *36*(4), 251-257.

Souchez, R., and J. Jouzel (1984), On the isotopic composition in δD and $\delta^{18}O$ of water and ice during freezing, *J Glaciol*, *30*(106), 369-372.

Stefels, J., G. Carnat, J. W. H. Dacey, T. Goossens, J. T. M. Elzenga, and J. L. Tison (2012), The analysis of dimethylsulfide and dimethylsulfoniopropionate in sea ice: Dry-crushing and melting using stable isotope additions, *Mar Chem*, *128-129*, 34-43.

Thomas, D. N., and G. S. Dieckmann (2002), Antarctic Sea Ice--a Habitat for Extremophiles, *Science*, *295*(5555), 641-644.

Thomas, D. N., S. Papadimitriou, and C. Michel (2010), Biogeochemistry of Sea Ice, in *Sea ice*, edited by D. N. Thomas and G. S. Dieckmann, pp. 425-467, Blackwell Publishing Ltd, UK.

Tison, J. L., A. Worby, B. Delille, F. Brabant, S. Papadimitriou, D. Thomas, J. de Jong, D. Lannuzel, and C. Haas (2008), Temporal evolution of decaying summer first-year sea ice in the Western Weddell Sea, Antarctica, *Deep-Sea Res Pt II*, *55*(8-9), 975-987.

Underwood, G. J. C., S. Fietz, S. Papadimitriou, D. N. Thomas, and G. S. Dieckmann (2010), Distribution and composition of dissolved extracellular polymeric substances (EPS) in Antarctic sea ice, *Marine Ecology Progress Series*, *404*, 1-19.

Vancoppenolle, M., C. M. Bitz, and T. Fichefet (2007), Summer landfast sea ice desalination of Point Barrow, Alaska: Modeling and observations, *Journal of Geophysical Research*, *112*(C04022).

Vancoppenolle, M., H. Goosse, A. de Montety, T. Fichefet, B. Tremblay, and J. L. Tison (2010), Modeling brine and nutrient dynamics in Antarctic sea ice: The case of dissolved silica, *Journal of Geophysical Research*, *115*.

Weeks, W. F. (2010), *On sea ice*, 664 pp., University of Alaska Press, Alaska.

Weingartner, T., K. Aagaard, R. Woodgate, S. Danielson, Y. Sasaki, and D. Cavalieri (2005), Circulation on the north central Chukchi Sea shelf, *Deep-Sea Research Part Ii-Topical Studies in Oceanography*, *52*(24-26), 3150-3174.

Weston, R. E. (1955), Hydrogen isotope fractionation between ice and water, *Geochim Cosmochim Ac*, *8*, 281-284.

Yamamoto-Kawai, M., E. C. Carmack, F. A. McLaughlin, and K. K. Falkner (2010), Oxygen isotope ratio, barium and salinity in waters around the North American coast from the Pacific to the Atlantic: Implications for freshwater sources to the Arctic throughflow, *J Mar Res*, *68*, 97-117.

List of figure captions

Figure 1 The study site. North of Barrow, Alaska, US.

Figure 2 The 10 sampling events (BRW1 to BRW10) referred to the continuous monitoring of air temperature, snow depth, and sea ice thickness at the Barrow sea ice observatory

Figure 3 (a) Ice cover temperature profile as obtained from thermistor chain measurements at the Barrow Sea ice Observatory versus (b) Ice core temperature profiles, for the 10 sampling events

Figure 4 (a) Snow thickness and ice depth shown with respect to the snow-ice interface. Ice texture is shown with different shading of bars (b) Thin section close-up at the transition level (15 cm to 17 cm) on BRW4. The arrows point to selected bubbles.

Figure 5 The evolution of (a) temperature, (b) salinity, (c) brine salinity, (d) brine volume fraction and (e) Rayleigh number computed with Freitag [1999] formulation of effective ice permeability. Plots are produced from "natural neighbors" interpolation of field measurements and derived data (dots).

Figure 6 Evolution of $\delta^{18}O$ and δD profiles in bulk sea ice and snow. Seawater value at BRW2 (typical seawater of the main growth period) is also shown.

Figure 7 Calculated δD changes in brine below 40 cm depth at BRW7, BRW8 and BRW10 (see Equation 4 in the text). δD in seawater, snow and brines are plotted for comparison.

Figure 8 NO_3^-, PO_4^{3-} and NH_4^+ concentrations in bulk ice (grey dots) compared to the dilution curve for seawater at BRW2, typical seawater of the main growth period. Nutrient concentrations in brine (white dots), seawater (triangles) and snow (squares) have been standardized at a salinity of 5 for comparison.

Figure 9 Evolution of the total chlorophyll-a (chl-a), total phaeopigment (phaeo), and percentage of small autotrophs

Figure 10 Individual chlorophyll-a (Chl-a) profiles at selected sampling events. The upper boxes refer to sea ice, the lower boxes to seawater. Gray stacked bars refer to chl-a of bulk ice or seawater, color points refer to chl-a in brines and snow

Figure 11 Evolution of Ar concentration ([Ar]) in bulk sea ice (dots) as compared to the solubility limits in sea ice calculated using temperature and salinity in brine (crosses) or temperature and salinity fixed at 0 °C and 34.5 respectively (empty dots). Deviation of [Ar] in bulk ice to the solubility limit indicates potential bubble content, while [Ar] in bulk ice at the solubility limit indicates that the gas is dissolved in brine.

Figure 12 Total chlorophyll-a (chl-a) plotted versus brine volume fraction (BrV). The dashed line at 5 % of brine volume fraction refers to the threshold for fluid permeability. The correlation coefficient is calculated with omission of the last 20 cm where the dynamic is clearly different from that in the rest of sea ice.

Figure 13 Schematic view of gas entrapment and evolution in sea ice through the 3 stages of brine dynamics described in the manuscript. After the entrapment, changes in temperature (T) and salinity (S), the presence of hydrophobic impurities and full-depth convection contribute to bubble nucleation. Bubbles could then migrate upward in permeable layers due to their buoyancy compared to the brines, while gas dissolved in brine would migrate as salt does, due to brine convection. Diffusion [*Loose et al.*, 2010] and the formation of superimposed ice layers may also control gas content in permeable sea ice.

Table 1 Synthesis on the evolution of the physical properties of landfast sea ice and their impacts on brine dynamics and atmosphere-ice-ocean exchanges of biogeochemical compound

			COLD stage	TRANSITION stage	WARM stage
Physical parameters			Texture	* Dominance of columnar ice	* Dominance of columnar ice	* Dominance of columnar ice, and superimposed ice formation at the ice surface
			Temperature, salinity	* Strong temperature gradient, c-shape salinity profile	* Nearly isothermal temperature profile, decrease of surface salinity	* Isothermal temperature profile, salinity close to 0 at the ice surface
			Brine salinity, brine volume fraction	* Unstable brine density profile associated with low ice permeability (brine volume fraction < 5 %) in the ice interior	* Unstable brine density profile associated with permeable ice cover (brine volume fraction > 5 %) at all depths	* Stable brine density profile associated with permeable ice cover (brine volume fraction > 10%) at all depths
			Ra	* 0 in the ice interior, 1 at the ice bottom	* Ra decreases from the ice surface (1 to 8) to the bottom (ca. 1)	* 0 at all depths
			Intepretation	**Active ice growth / Sea-ice bottom-layer convection**	**Late ice growth / Brine drainage or Full-depth convection**	**Ice melt / No convection or brine stratification**
Biogeochemical compounds	***Dissolved***	***Abiotic***	δD, $\delta^{18}O$	* Physical control only (e.g., parent water mass, isotopic fractionation)	* δD_{brine} approaches the values in seawater	* Decrease of surface δD_{brine} due to snow melt
		Biotic	Nutrients	* Both physical (e.g., incorporation and rejection) and biological controls (e.g., remineralisation).	* Slight decrease in bulk ice nutrient concentration	* Slow/no exchange between brine and under-ice water, but potential input of NO_3^- through snow melt

	Particle	Chl-a	* Physical parameters constrain algal distribution (e.g., low temperature, high brine salinity and limited nutrient supply)	* Drainage of micro-organisms from sea ice to under-ice water with rapid resumption and potential changes in species	* Algal growth under low nutrient concentration conditions
	Gaseous	Ar	* Gas bubble formation allows Ar accumulation in sea ice, large Ar supersaturation compared to Ar solubility in ice is observed	* Further Ar accumulation	* No more supersaturation. Gas should have escaped for brine volume fraction approaching 7.5 to 10 %
	Interpreation in parallel with the physical processes		**Sea ice is mainly impermeable. The ice interior acts as a close system, which allows accumulations of Ar and NH_4^+. Physical constrains on algae are strong.**	**Sea ice permeability increases (semi-open system) and allows important exchanges with the under-ice water through brine drainage. While dissolved compounds and particles are partially transfered to the under-ice water, gas further accumulates.**	**Sea ice permeability further increases (open system). The exchanges between brine and seawater slows down due to brine stratification, but gas exchanges between brine and the atmosphere is possible. Snow/ice melt and superimposed ice formation locally impact the concentrations of biogeochemical compounds.**

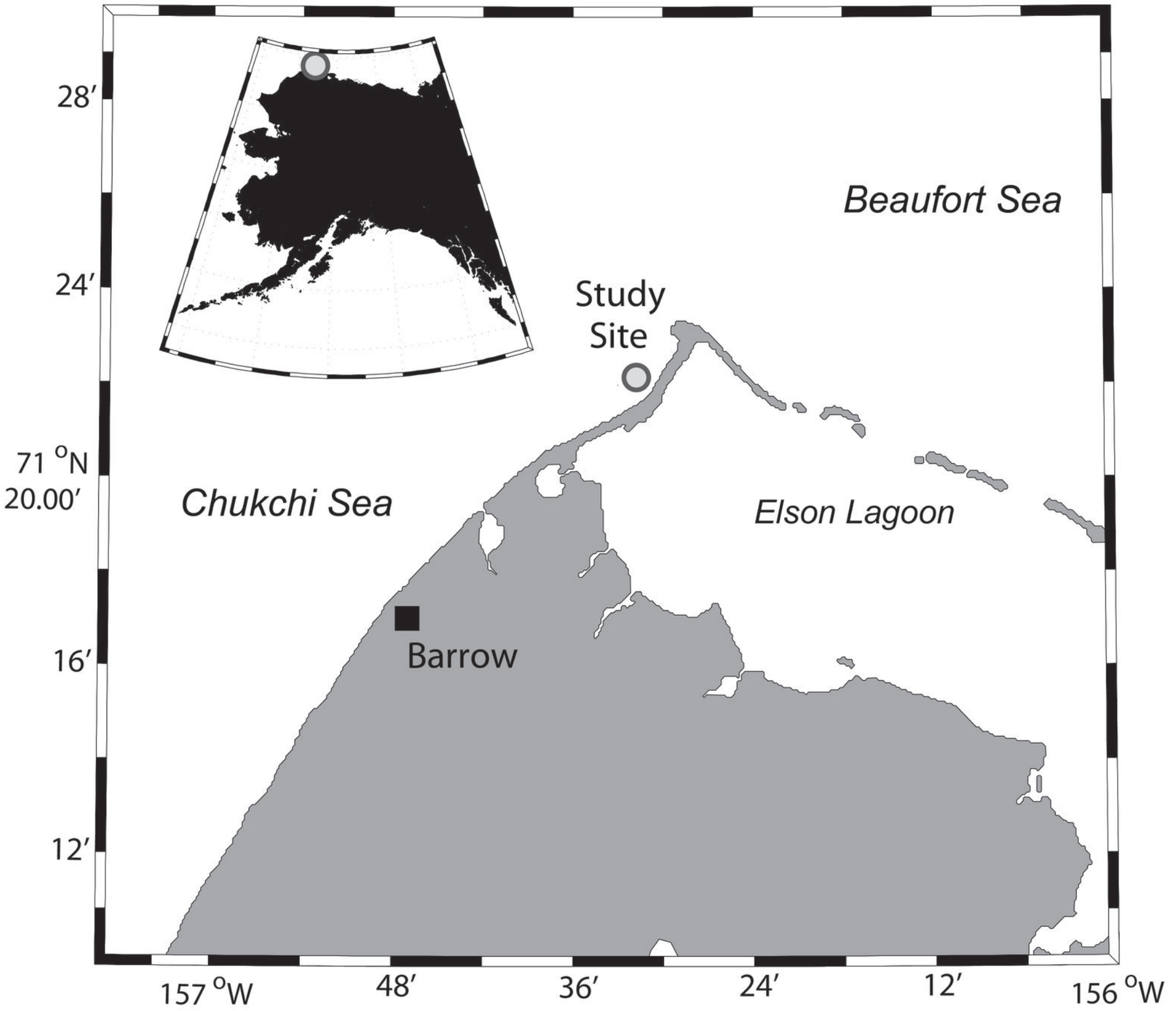
28′
24′
71 °N
20.00′
16′
12′
157 °W
48′
36′
24′
12′
156 °W
Beaufort Sea
Study
Site
Chukchi Sea
Elson Lagoon
Barrow

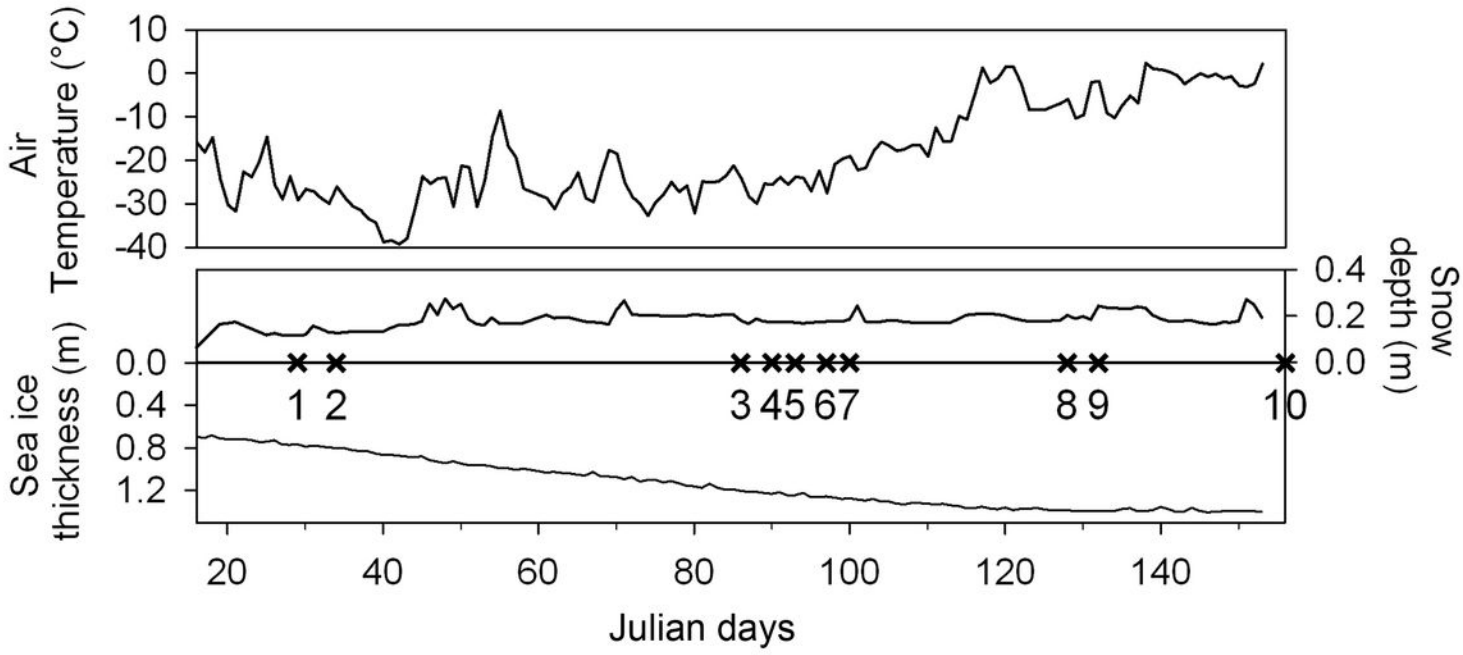

BRW1	January 29	**BRW3**	March 27	**BRW5**	April 4	**BRW7**	April 10	**BRW9**	May 12
BRW2	February 3	**BRW4**	March 31	**BRW6**	April 7	**BRW8**	May 8	**BRW10**	June 5

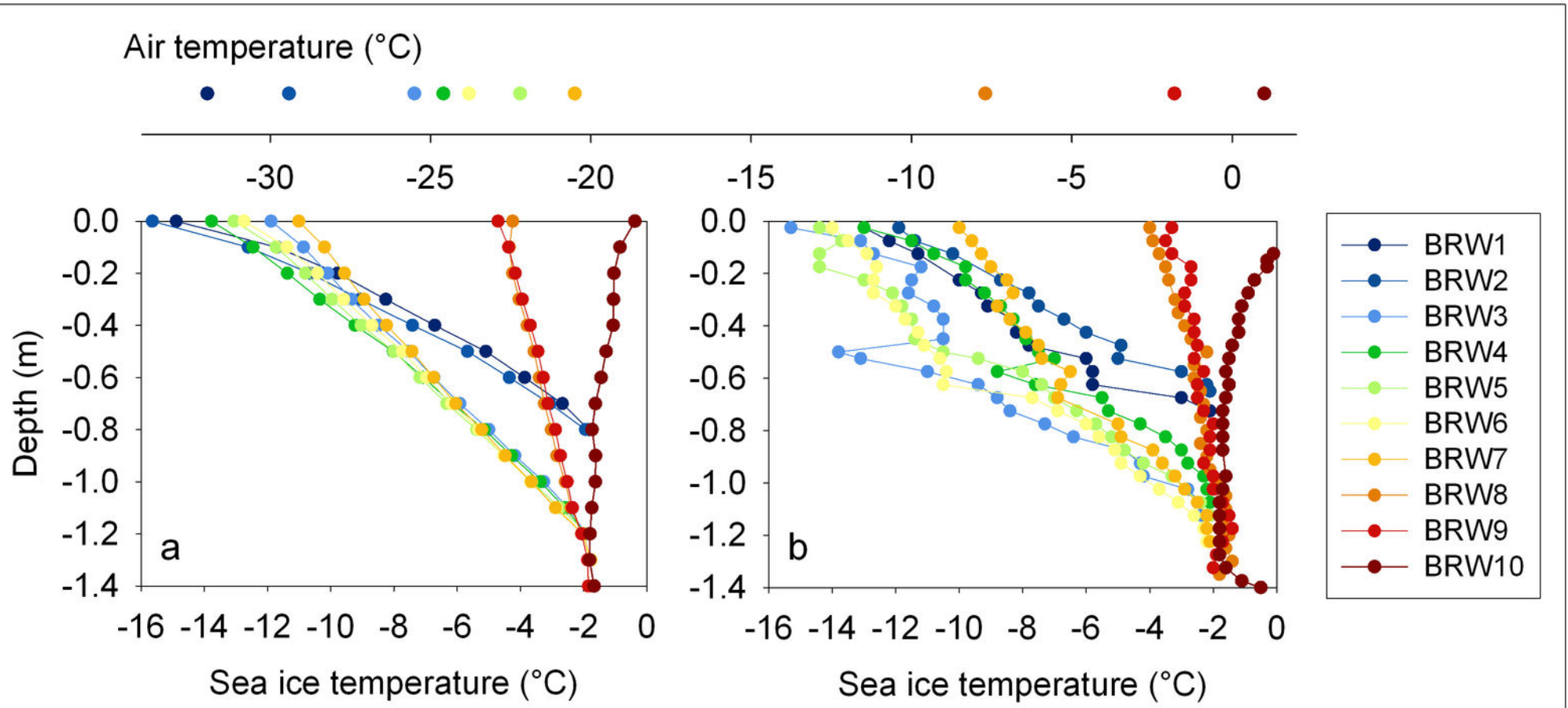
Air temperature (°C)
-30
-25
-20
-15
-10
-5
0
Depth (m)
0.0
-0.2
-0.4
-0.6
-0.8
-1.0
-1.2
-1.4
a
b
-16 -14 -12 -10 -8 -6 -4 -2 0
Sea ice temperature (°C)
Sea ice temperature (°C)
BRW1
BRW2
BRW3
BRW4
BRW5
BRW6
BRW7
BRW8
BRW9
BRW10

a

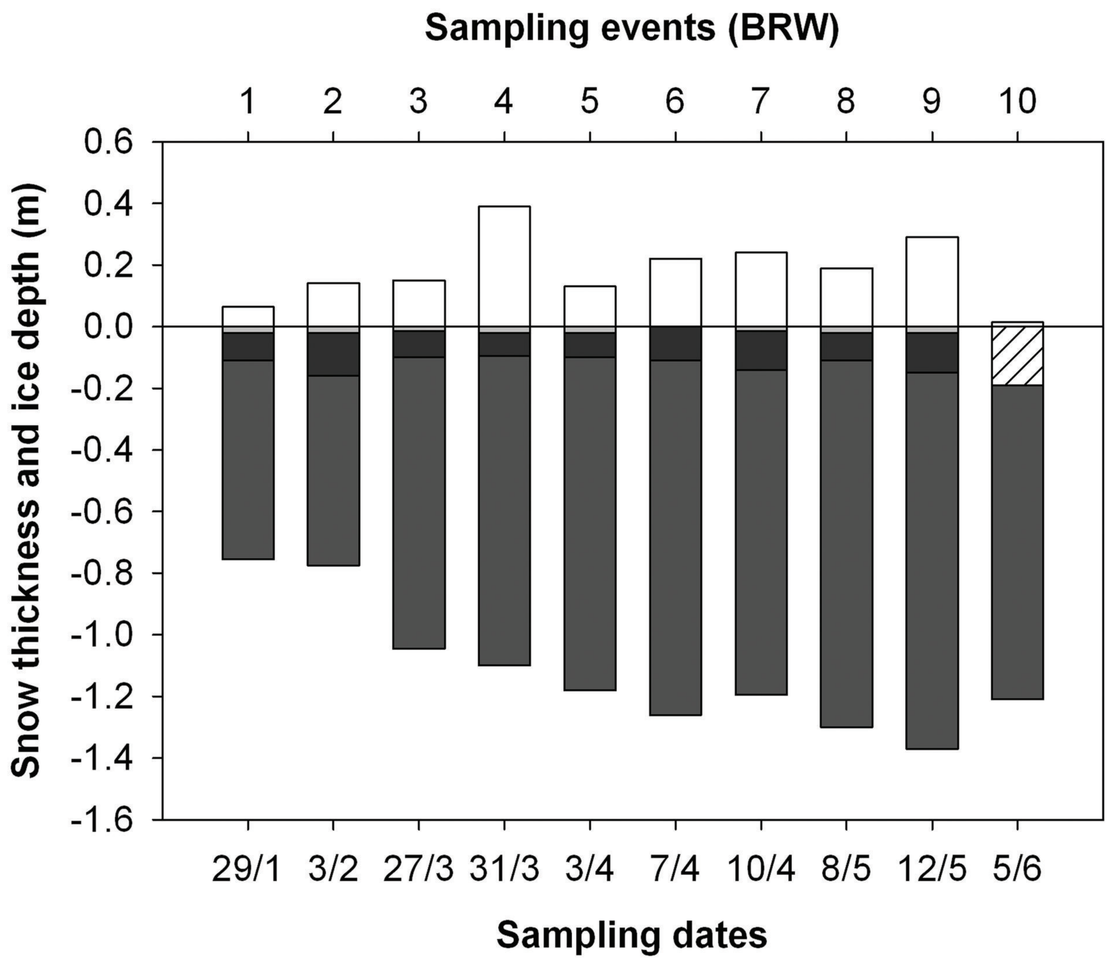

Snow

Columnar ice

Granular ice

Transition ice

Porous ice interleaved with superimposed ice layers

b

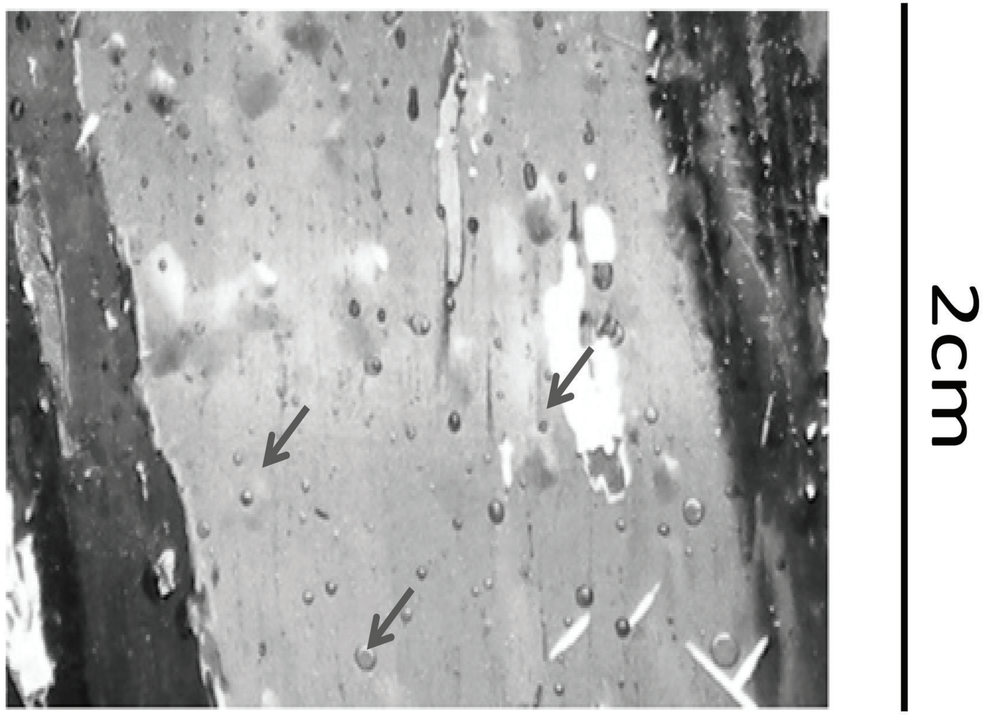

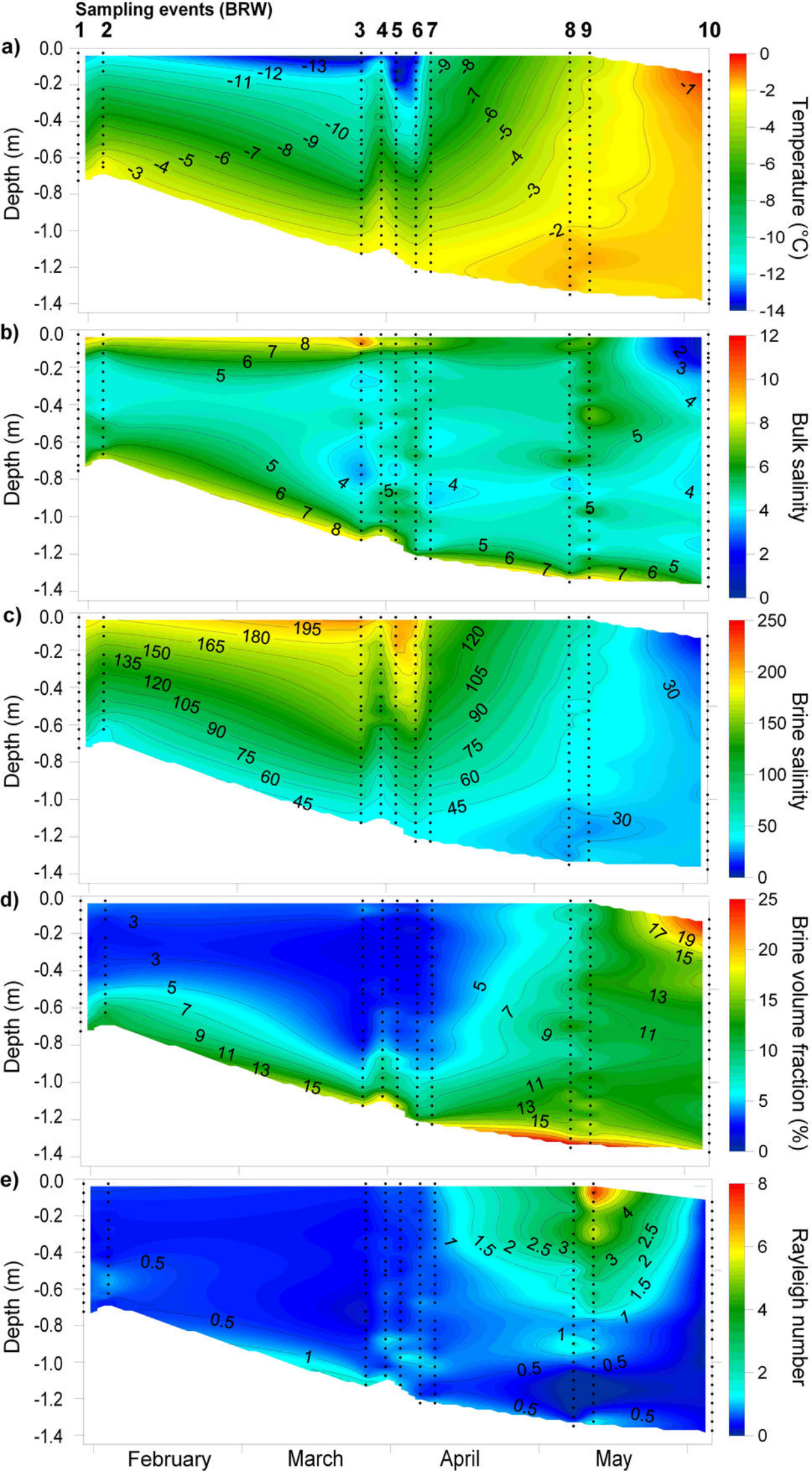
Sampling events (BRW)
1 2 3 4 5 6 7 8 9 10
a)
b)
c)
d)
e)
Depth (m)
0.0
-0.2
-0.4
-0.6
-0.8
-1.0
-1.2
-1.4
Temperature (°C)
0 -2 -4 -6 -8 -10 -12 -14
Bulk salinity
0 2 4 6 8 10 12
Brine salinity
0 50 100 150 200 250
Brine volume fraction (%)
0 5 10 15 20 25
Rayleigh number
0 2 4 6 8
February
March
April
May

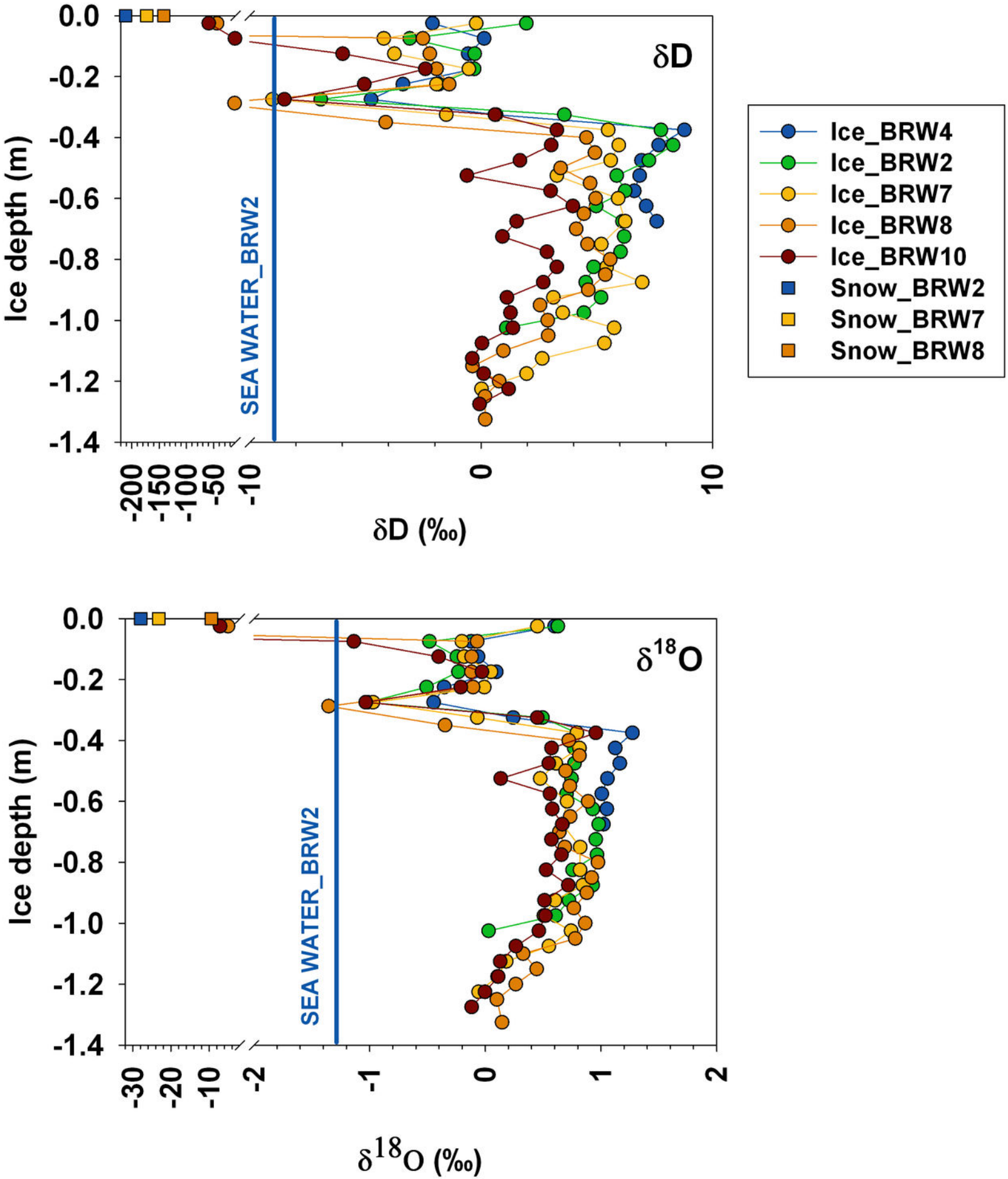
δD
SEA WATER_BRW2
Ice depth (m)
0.0
-0.2
-0.4
-0.6
-0.8
-1.0
-1.2
-1.4
-200
-150
-100
-50
-10
0
10
δD (‰)
Ice_BRW4
Ice_BRW2
Ice_BRW7
Ice_BRW8
Ice_BRW10
Snow_BRW2
Snow_BRW7
Snow_BRW8
δ18O
SEA WATER_BRW2
Ice depth (m)
-30
-20
-10
-2
-1
0
1
2
δ18O (‰)

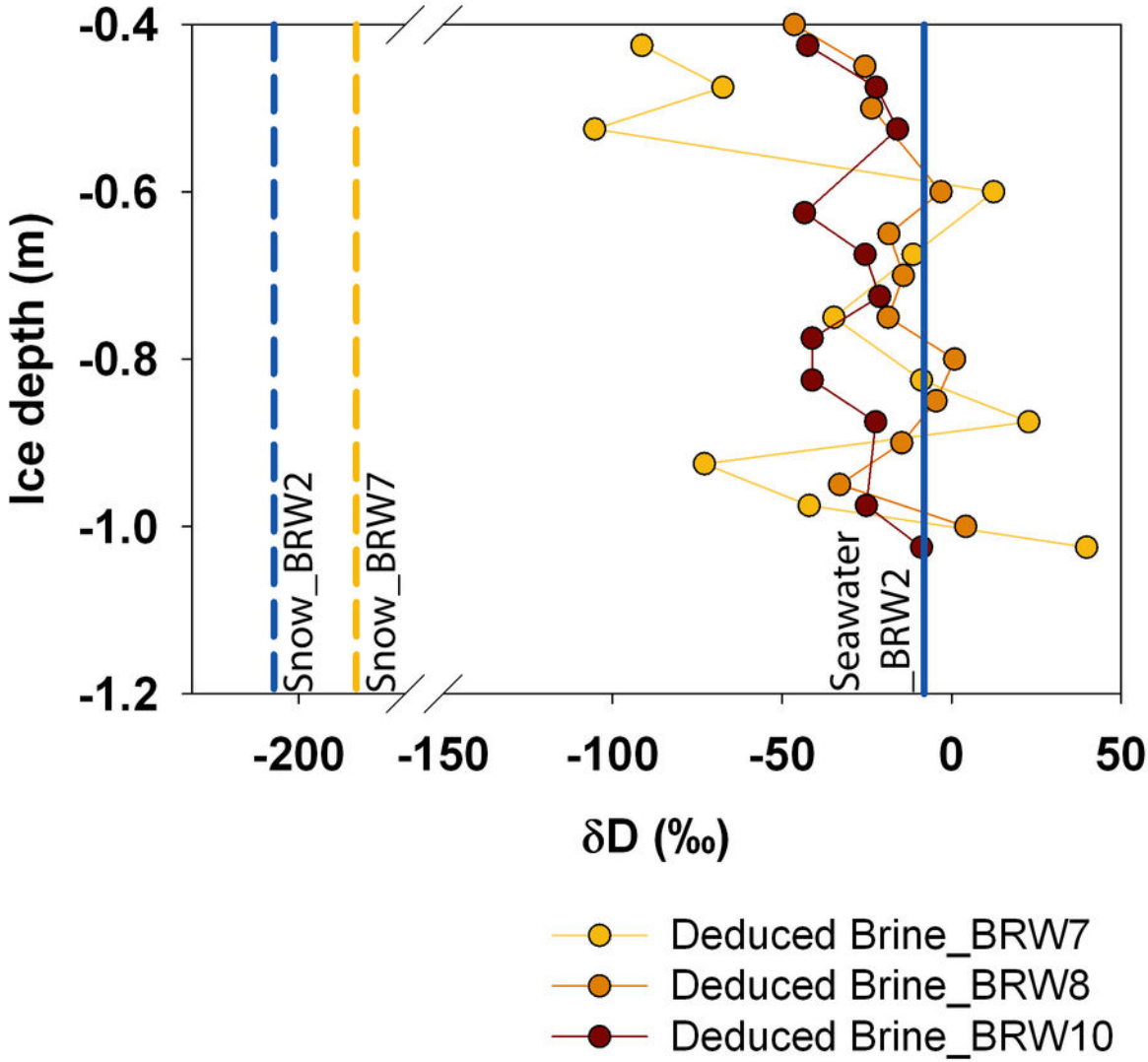
-0.4
-0.6
-0.8
-1.0
-1.2
Ice depth (m)
-200
-150
-100
-50
0
50
δD (‰)
Snow_BRW2
Snow_BRW7
Seawater _BRW2
Deduced Brine_BRW7
Deduced Brine_BRW8
Deduced Brine_BRW10

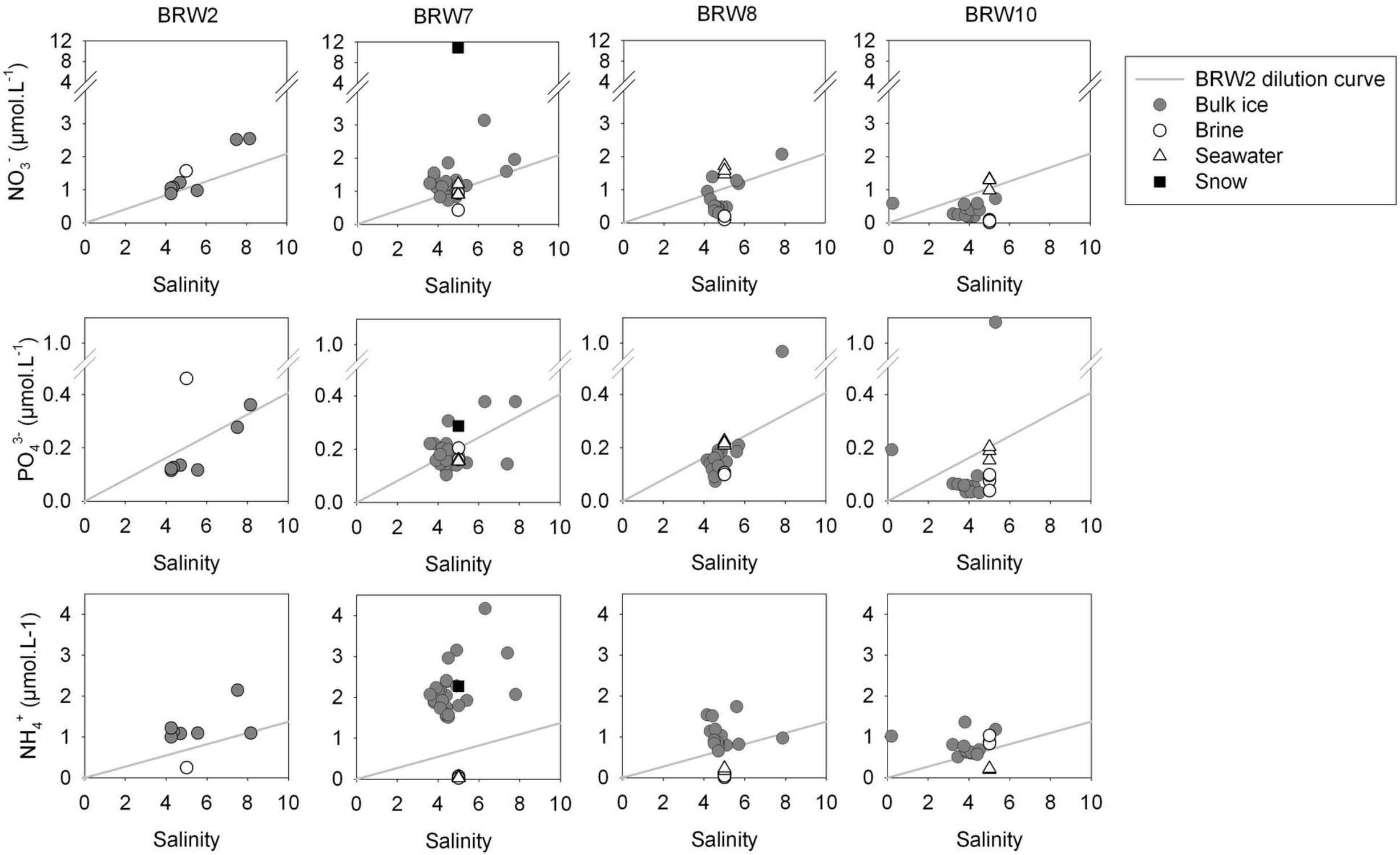
BRW2
BRW7
BRW8
BRW10
NO_3^- (µmol.L^{-1})
PO_4^{3-} (µmol.L^{-1})
NH_4^+ (µmol.L-1)
Salinity
BRW2 dilution curve
Bulk ice
Brine
Seawater
Snow

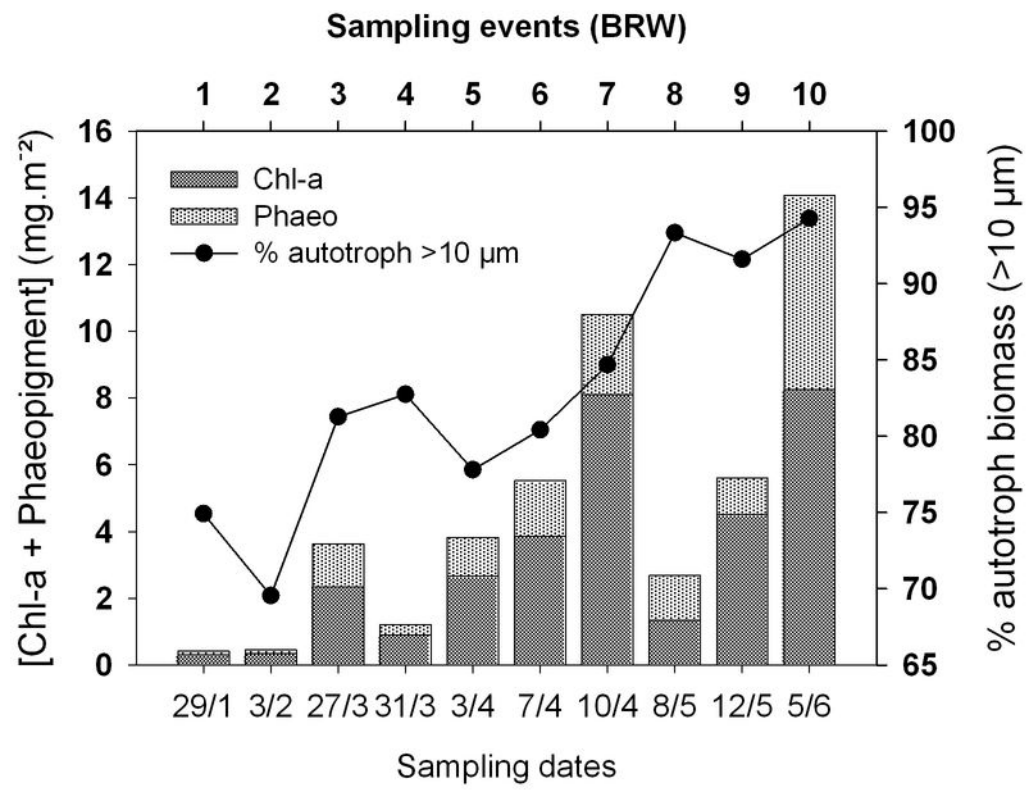
Sampling events (BRW)
1
2
3
4
5
6
7
8
9
10
[Chl-a + Phaeopigment] (mg.m-2)
16
14
12
10
8
6
4
2
0
Chl-a
Phaeo
% autotroph >10 µm
100
95
90
85
80
75
70
65
% autotroph biomass (>10 µm)
29/1
3/2
27/3
31/3
3/4
7/4
10/4
8/5
12/5
5/6
Sampling dates

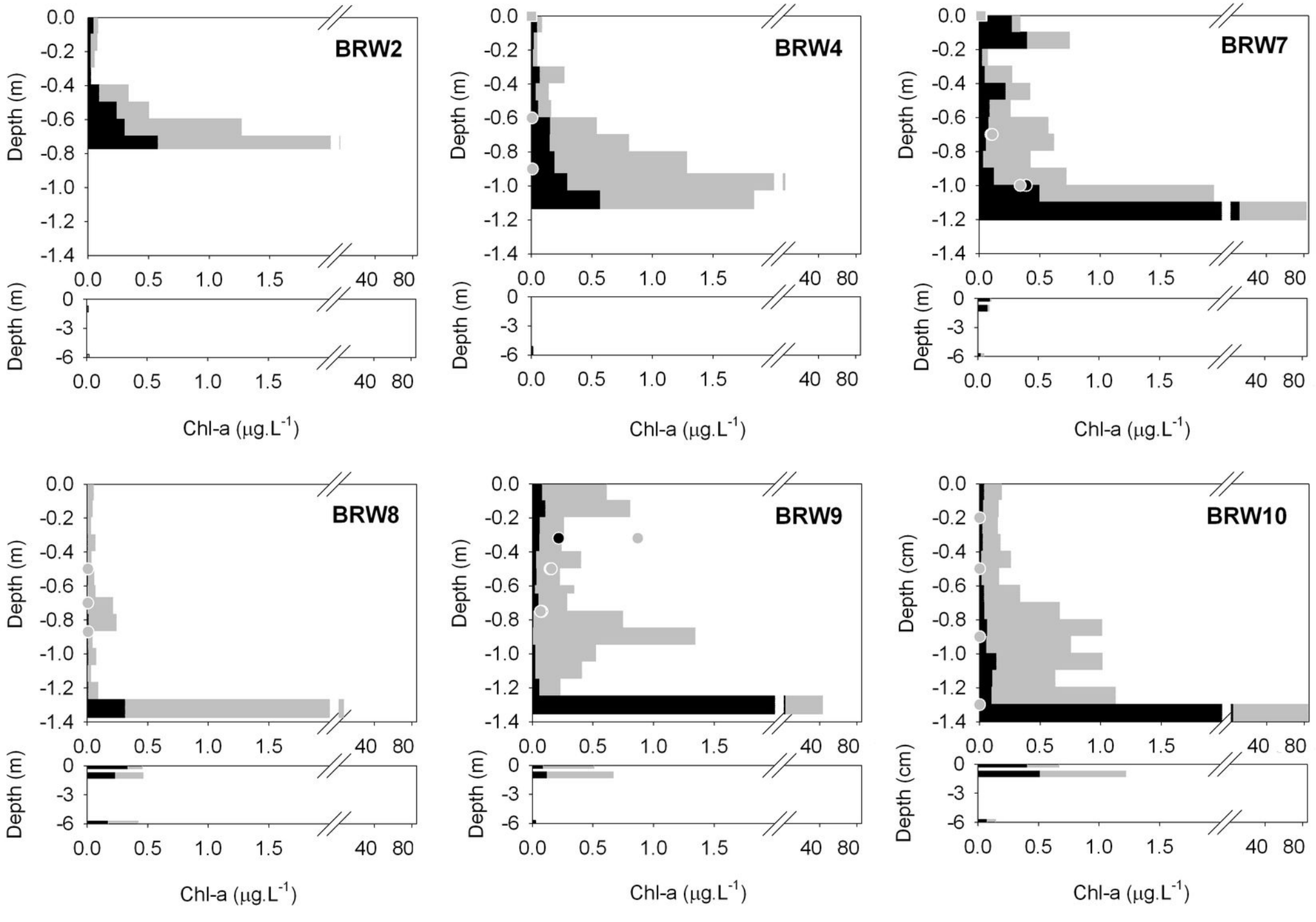
BRW2
BRW4
BRW7
BRW8
BRW9
BRW10
Depth (m)
Depth (cm)
Chl-a (µg.L-1)
0,8 - 10 µm (ice/seawater)
> 10 µm (ice/seawater)
0,8 - 10 µm (brines)
> 10 µm (brines)
0,8 - 10 µm (snow)
> 10 µm (snow)

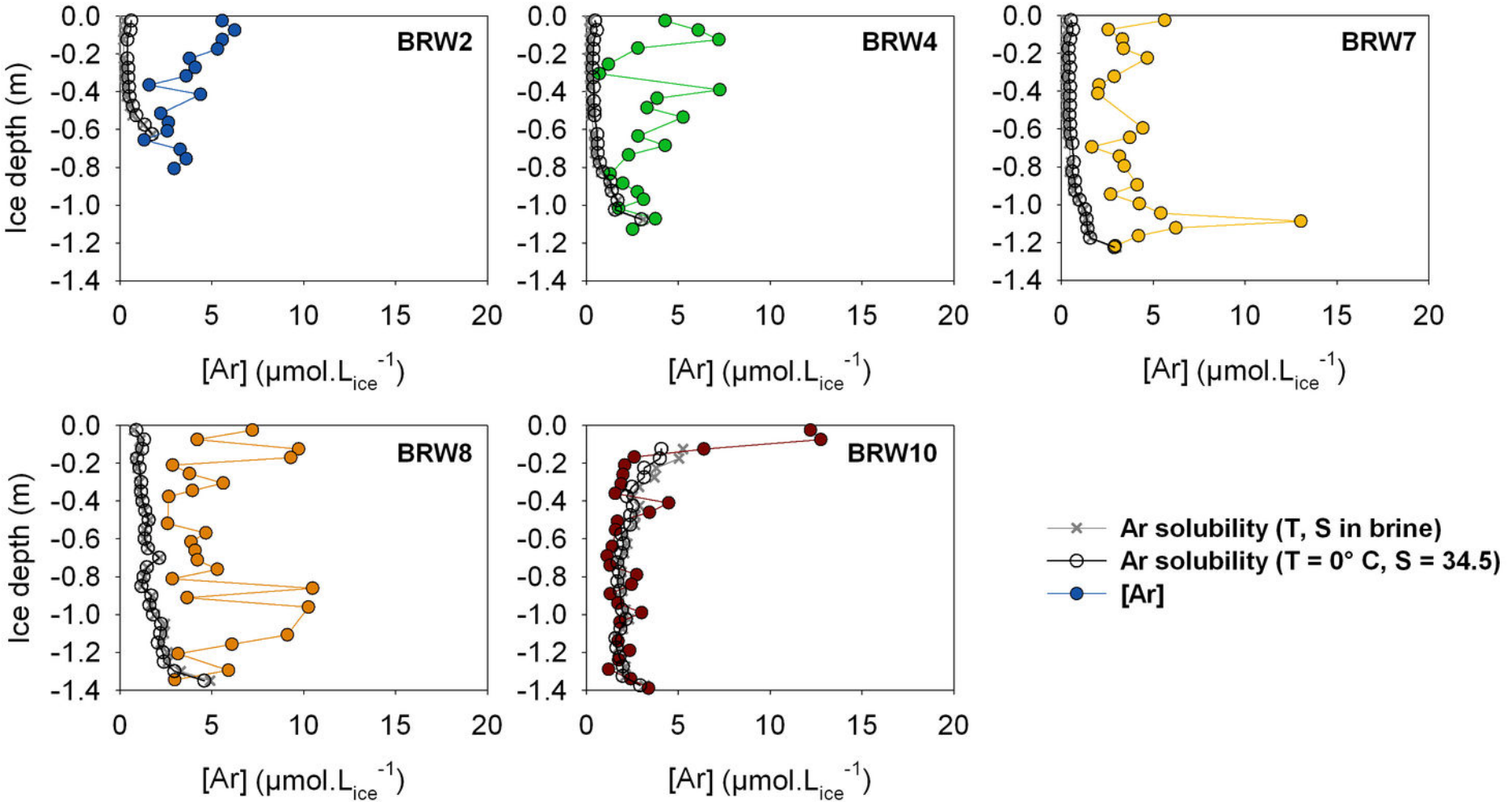
BRW2
BRW4
BRW7
BRW8
BRW10
Ice depth (m)
0.0
-0.2
-0.4
-0.6
-0.8
-1.0
-1.2
-1.4
0
5
10
15
20
[Ar] (µmol.L$_{ice}^{-1}$)
Ar solubility (T, S in brine)
Ar solubility (T = 0° C, S = 34.5)
[Ar]

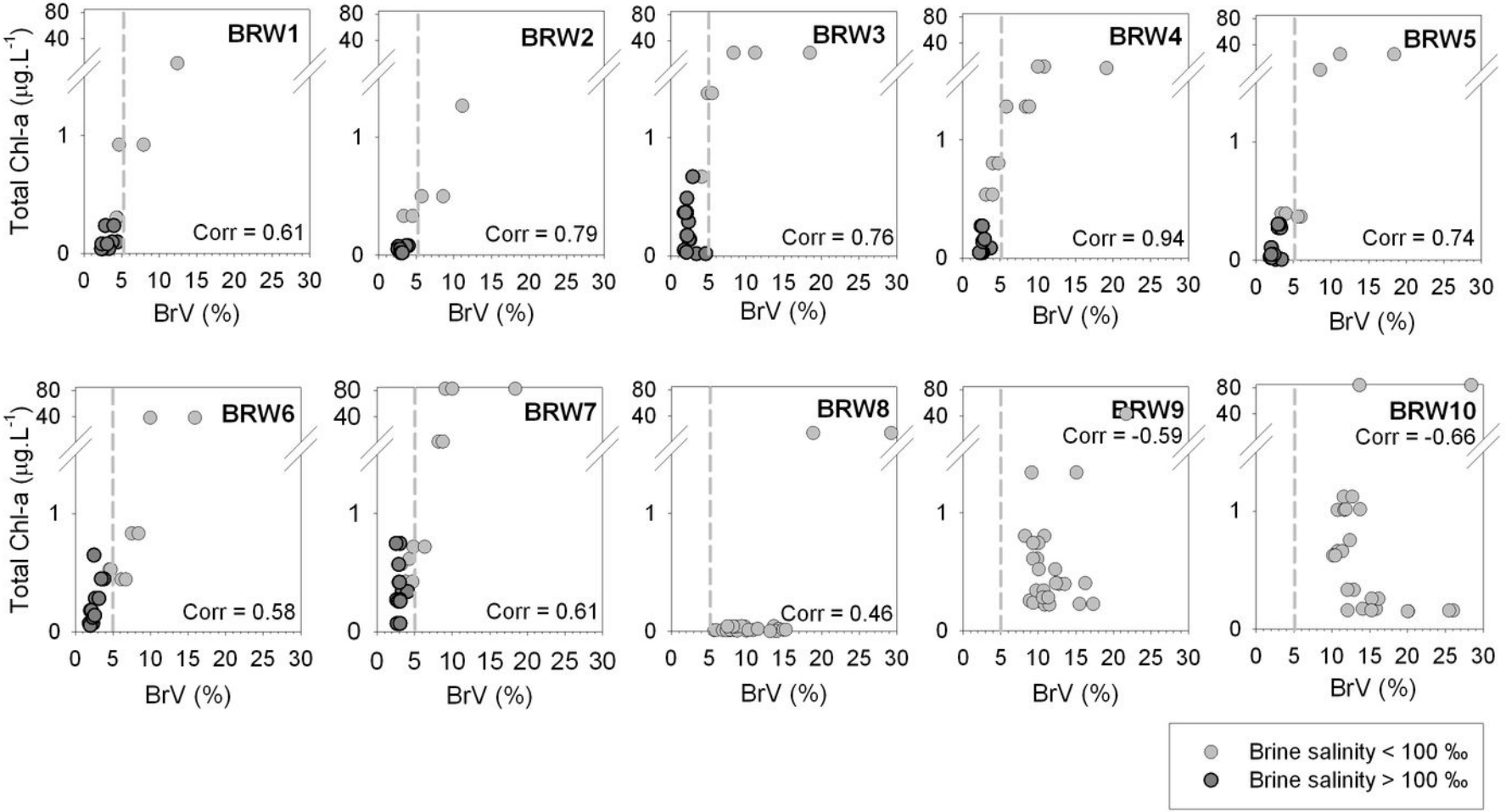
BRW1
BRW2
BRW3
BRW4
BRW5
BRW6
BRW7
BRW8
BRW9
BRW10
Corr = 0.61
Corr = 0.79
Corr = 0.76
Corr = 0.94
Corr = 0.74
Corr = 0.58
Corr = 0.61
Corr = 0.46
Corr = -0.59
Corr = -0.66
Total Chl-a (µg.L-1)
BrV (%)
0
1
40
80
0 5 10 15 20 25 30
Brine salinity < 100 ‰
Brine salinity > 100 ‰

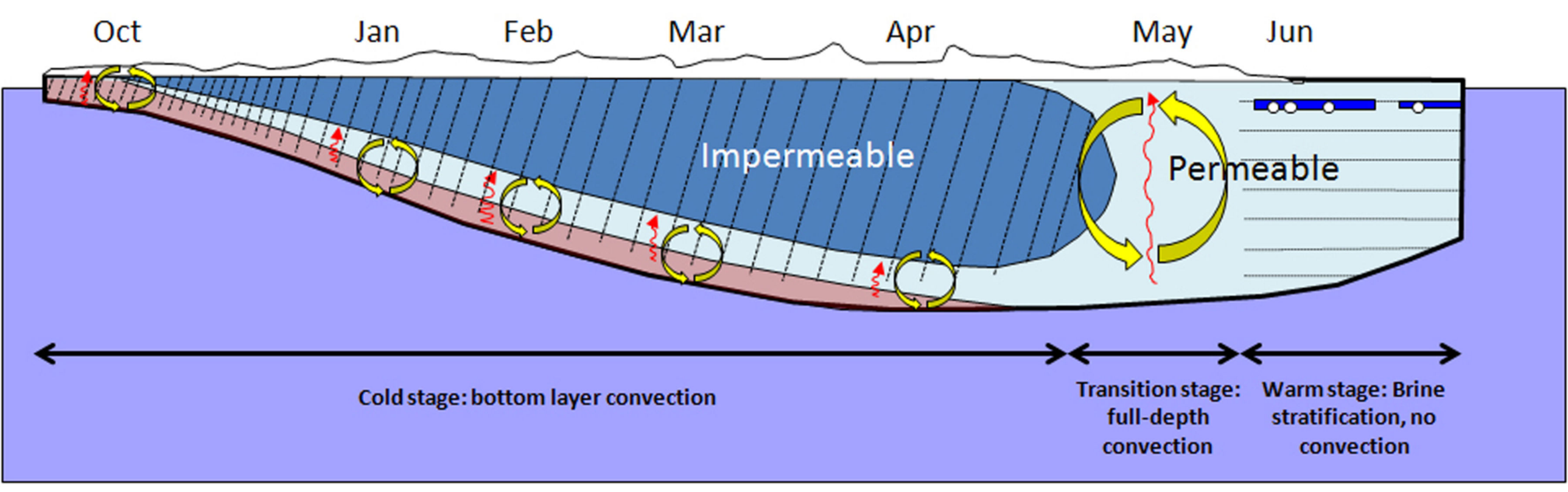

Initial entrapment → Bubble Nucleation

Drivers

1. **T, S**
2. **Hydrophobic impurities**
3. **Full-depth convection**

Bubble Nucleation → Upward gas migration in permeable* layer due to Buoyancy

Bubble Nucleation → Convection with brines affect dissolved gas and salt

Diffusion and superimposed ice layer control gas content in stratified brine system

*Permeability threshold for brine: brine volume fraction > 5% ; permeability threshold for gas: brine volume fraction > 7.5 %